Eur. Phys. J. D **12**, 61–93 (2000)

THE EUROPEAN PHYSICAL JOURNAL D

EDP Sciences

Metrology of the hydrogen and deuterium atoms: Determination of the Rydberg constant and Lamb shifts

B. de Beauvoir[1], C. Schwob[1], O. Acef[2], L. Jozefowski[1], L. Hilico[1,a], F. Nez[1], L. Julien[1], A. Clairon[2], and F. Biraben[1,b]

[1] Laboratoire Kastler Brossel, École Normale Supérieure et Université Pierre et Marie Curie[c], 4 place Jussieu, 75252 Paris Cedex 05, France

[2] Laboratoire Primaire du Temps et des Fréquences, Bureau National de Métrologie-Observatoire de Paris, 61 avenue de l'Observatoire, 75014 Paris, France

Received 9 March 2000

Abstract. We present a detailed description of several experiments which have been previously reported in several letters: the determination of the 1S Lamb shift in hydrogen by a comparison of the frequencies of the 1S–3S and 2S–6S or 2S–6D two-photon transitions, and the measurement of the 2S–8S/D and 2S–12D optical frequencies. Following a complete study of the lineshape of the two-photon transitions, we provide the updated values of these frequencies which have been used in the 1998 adjustment of the fundamental constants. From an analysis taking into account these results and several other precise measurements by other authors, we show that the optical frequency measurements have superseded the microwave determination of the 2S Lamb shift and we deduce optimized values for the Rydberg constant, $R_\infty = 109\,737.315\,685\,50(84)$ cm^{-1} (relative uncertainty of 7.7×10^{-12}) and for the 1S and 2S Lamb shifts $L(1S) = 8\,172.840(22)$ MHz and $L(2S–2P) = 1\,057.8450(29)$ MHz (respectively, 8 183.970(22) MHz and 1 059.2341(29) MHz for deuterium). These are now the most accurate values available.

PACS. 06.20.Jr Determination of fundamental constants – 21.10.Ft Charge distribution – 31.30.Jv Relativistic and quantum electrodynamic effects in atoms and molecules

1 Introduction

Over the past two decades the absolute measurement of wavelengths or frequencies of hydrogen has been continuously improved with the aim of determining the Rydberg constant and testing quantum electrodynamics calculations. With the interferometric measurements, the relative accuracy was in the range of one part in 10^{10}. A review of these results is provided in reference [1]. Recently, the interferometric measurements have been superseded by accurate optical frequency ones. The latter make use of frequency-multiplication chains which link the measured frequency, *via* intermediate standard lasers, to the caesium clock. With this method, Hänsch and collaborators have measured the optical frequency of the 1S–2S two-photon transition with an accuracy better than 3.4×10^{-13} [2,3]. In our group, we have studied the 2S–nS and 2S–nD two-photon transitions. In 1993, we measured the optical frequencies of the $2S_{1/2}$–$8S_{1/2}$, $2S_{1/2}$–$8D_{3/2}$ and $2S_{1/2}$–$8D_{5/2}$ transitions in hydrogen with a frequency chain using two standard lasers (the iodine stabilized and the methane stabilized helium-neon lasers) and obtained a precision in the range of 10^{-11} [4,5]. In 1996, we remade these measurements in hydrogen and deuterium with an accuracy better than one part in 10^{11} [6]. We used a new frequency chain with a new standard laser, namely a diode laser at 778 nm stabilized on the 5S–5D two-photon transition of rubidium (LD/Rb laser). The frequency of this standard was measured with a frequency chain at the *Laboratoire Primaire du Temps et des Fréquences* (LPTF) [7]. More recently, in order to check these 2S–8S/D frequency measurements, we have built a new chain to measure the frequencies of the 2S–12D transitions in hydrogen and deuterium [8]. In parallel, we have taken advantage of our experimental setup on the 2S–nS/D transitions to deduce the Lamb shift of the 1S level *via* a comparison of the frequencies of the 1S–3S and 2S–6S/D transitions [9].

The aim of this paper is to relate in detail these experiments. Section 2 describes our apparatus for the observation of the 2S–nS and 2S–nD transitions, which is the corner stone of our hydrogen experiments. The Doppler free two-photon transitions, in the range 750–820 nm, are induced by a highly stable titanium-sapphire laser. To reduce the transit time broadening, we use an atomic beam colinear with the laser beam. Section 3 is devoted to the line shape analysis of the 2S–nS/D transitions. We follow

[a] Affiliated with Université d'Évry Val d'Essonne, France.

[b] e-mail: biraben@spectro.jussieu.fr

[c] Laboratoire associé au CNRS, UMR 8552.

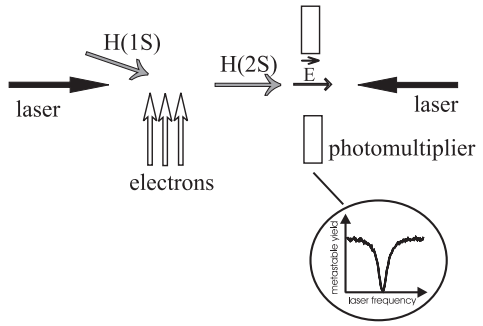

Fig. 1. Experimental geometry of laser and atom beams to observe the 2S–nS and 2S–nD two-photon transitions. When the laser frequency is scanned over the resonance, we observe a decrease of the metastable yield (see the inset).

the same procedure as in our previous work [10–12]. We calculate the two-photon transition probability for a single atom and average over all the possible trajectories. In our recent calculations, we have taken into account the small hyperfine structure of the D levels, photoionisation effects, the small deviation of the atomic trajectories due to the light forces, as well as the second-order Doppler effect. We present the data analysis procedure and calculate the corrections due to stray electric fields. The optical frequency measurements are presented in Section 4. We describe the rubidium optical frequency standard and the various frequency chains used to measure the 2S–8S/D and 2S–12D transitions. Finally, we give the up-to-date results, which take into account the best line shape analysis and the most recent measurements of the optical frequency standards. The comparison of the 1S–3S and 2S–6S/D frequencies is described in Section 5. Finally, in Section 6, we analyse all these results to deduce the Rydberg constant and the Lamb shifts of the 1S and 2S levels. We show that the optical frequency measurements have superseded the radiofrequency measurements of the 2S Lamb shift and, using a least squares procedure which takes into account all the precise measurements in hydrogen and deuterium, we deduce a value of the Rydberg constant with a relative uncertainty of 7.7×10^{-12}.

2 Spectroscopy of the 2S–nS and 2S–nD transitions

2.1 Method

The principle of the experiment has been described previously [10]. The experimental geometry is illustrated in Figure 1. A metastable atomic beam is formed by electronic excitation of a 1S hydrogen atomic beam. Due to the inelastic collision with the electron, the atomic trajectory is deviated by an angle of about 20°. We use this deviation to make colinear, after the collision, the 2S atomic beam with the laser beams. At the end of the atomic beam we monitor the metastable yield: an electric field quenches the metastable state and we detect the Lyman-α fluorescence. When the laser frequency is in resonance with the

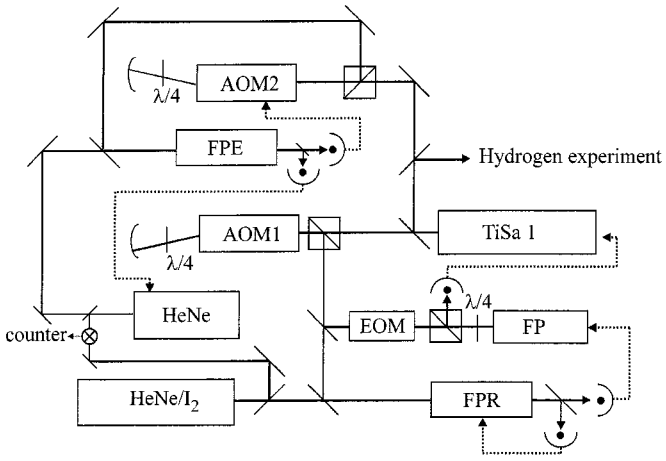

Fig. 2. Experimental setup for the frequency stabilisation of the titanium-sapphire laser. The explanations are given in the text (TiSa1: titanium-sapphire laser, HeNe/I_2: iodine stabilized helium-neon laser, He–Ne: auxiliary helium-neon laser, AOM1 and AOM2: acousto-optic modulators, EOM: electro-optic modulator, FP, FPR and FPE: Fabry-Perot cavities).

2S–nS/D transition, the atoms in the nS or nD states undergo a radiative cascade towards the 1S state in a proportion of about 95%. It occurs an optical quenching of the metastable level before the detection region and the optical excitation can be detected *via* the corresponding decrease of the 2S beam intensity (see Fig. 1).

2.2 Laser source

To induce the optical excitation, we use a home-made titanium-sapphire laser which has been described previously [13]. With a pump power of 13 W (from a Spectra-Physics 2030 argon ion laser), the single frequency output power is about 2 W at 800 nm. For some experiments [4,5, 8], we use a second titanium-sapphire laser with the same pump laser and the available power is reduced to about 1 W. For the high-resolution hydrogen spectroscopy, we require a narrow laser bandwidth and a good long term frequency stability. The frequency stabilisation set-up is shown in Figure 2. The short term and long term stability are assured with two Fabry-Perot cavities, labelled FP and FPR respectively. The principle of this stabilisation arrangement is to lock the titanium-sapphire laser on the FP cavity, the FP cavity to the FPR cavity and, finally, the FPR cavity to an iodine stabilized helium-neon laser. A secondary laser beam from the titanium-sapphire laser is splitted after a double pass through an acousto-optic modulator (model 3200 from Crystal Technology at 200 MHz, labelled AOM1 in Fig. 2) and sent on the FP and FPR cavities. The FP cavity (free spectral range 600 MHz and finesse of about 400) is placed in a robust vacuum box (wall thickness of 2 cm) and carefully isolated from the external vibrations[13]. To reduce the frequency jitter, the laser is locked, in a first step, on the FP cavity. We use an FM sideband method [14]: the laser beam sent in the FP cavity is phase modulated at about

15 MHz with an electro-optic modulator (Gsänger PM25, labelled EOM in Fig. 2). From the modulation detected on the beam reflected by the FP cavity, we extract an error signal which controls the piezoelectric and electro-optic transducers monitoring the length of the laser cavity. Thanks to this servo-loop, the frequency jitter is reduced from 500 kHz (free running laser) to about 2 kHz [13].

The long term stability is guaranteed by the reference Fabry-Perot cavity FPR. This cavity is very stable. It consists of a 50 cm long zerodur spacer and two silver coated mirrors, one flat and one spherical (60 cm curvature radius). Its finesse is about 75 at 633 nm and 120 at 800 nm. A piezoelectric transducer (PZT) moves the flat mirror thanks to a mechanical construction (made in fused silica) which avoid the rotation of the mirror (the principle is to deform a parallelogram) [15]. This cavity is also placed in a vacuum box with the same design that for the FP cavity. To obtain the long term stability, the FPR cavity is irradiated simultaneously by an iodine stabilized helium-neon laser and a part of the titanium-sapphire laser (after the double pass in the acousto-optic modulator). A first servo-loop locks the FPR length to the helium-neon wavelength (we use the 10 kHz frequency modulation of the helium-neon laser). As the zerodur spacer is very stable, we have always used, since ten years, the same fringes of the FPR cavity (1 580 868 or 1 580 869 following the PZT voltage). The length of the FPR cavity is also modulated (frequency of about 4.2 kHz). This modulation is detected on the transmission of the titanium-sapphire laser and a second servo-loop locks the length of the FP cavity to the FPR cavity. To scan the laser frequency, we sweep the frequency of the radiofrequency wave which drives the acousto-optic modulator. With this arrangement, the lengths of the two FP and FPR cavities are fixed and the commutation time of the laser frequency is only limited by the bandwidth of the first servo-loop on the FP cavity (about 50 kHz). An other advantage of this system with two cavities is that the accuracy is given by the servo-loop on the FPR cavity. This accuracy is better than the accuracy of the first servo-loop on the FP cavity for two reasons: (i) the modulation of the FPR cavity is small (about 10% of the cavity bandwidth) and the error signal is less perturbated by the transverse modes of the FPR cavity which appear when the laser beam is not perfectly mode matched on the cavity, (ii) the transmission signal of the cavity is an Airy function which has approximatively a symmetric Lorentzian profile. It is not the case for the servo-loop on the FP cavity which is made with the reflected beam by the cavity. In this case, the profile of the resonance of the cavity can be dissymetric because of the losses of the mirrors (it is the sum of an absorption and a dispersion shapes due to the phase shift between the first reflection on the input mirror and the beam which comes out of the cavity) [15].

Thanks to our optical frequency measurements (see Sect. 4), we have tested the metrological features of this laser system. For instance, we have very often measured the optical frequency of the fringe 1 286 174 of the FPR cavity which is close to the 2S–8S/D two-photon transition

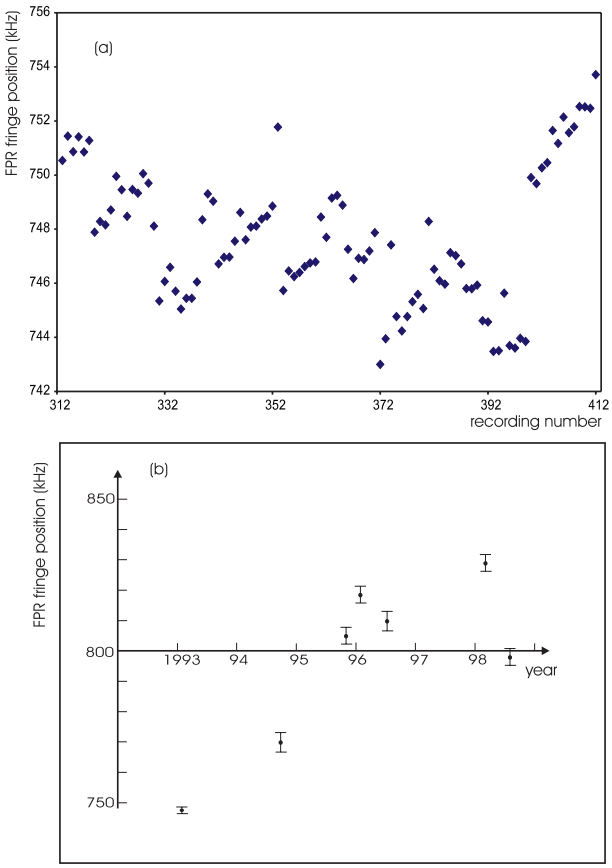

Fig. 3. Absolute frequency of the fringe 1 286 174 of the FPR cavity when the fringe 1 580 868 is locked to the d line of the iodine stabilized He–Ne laser. The values are in kHz and we have subtracted 385 325 GHz. (a) Measurements made in 1993: each point is the value obtained during a 20 minutes recording of the 2S–8S/D transitions in hydrogen. The measurements were made during about two weeks. The mean value is 385 325 000 747.7(2.5) kHz. (b) Drift of the fringe frequency on the period 1993–1998.

in hydrogen. The results are reported in Figures 3a and 3b. Figure 3a shows a series of measurements made in 1993 [5]. Each point is the mean of a 20 minutes recording (see Sect. 2.3). The standard deviation of these data is about 2.5 kHz, *i.e.* a day-to-day stability of 7×10^{-12}. Figure 3b shows the results since several years. During five years, we have observed a frequency drift of about 100 kHz which is perhaps due to an aging of the silver coating.

We use also several other interferometers to control the wavelength of the laser: a lambdameter (typical accuracy 10^{-3} nm), a 3 cm Fabry-Perot cavity (placed in a vacuum box and scanned by pressure variation) and an other, 50 cm long, Fabry-Perot cavity (labelled FPE in Fig. 2). This cavity has the same design that the FPR cavity, except that there is no PZT. To know the length of the FPE cavity, an auxiliary He–Ne laser is locked on a fringe of this cavity and we measure the beat frequency between the two He–Ne lasers. Simultaneously, a secondary beam of the titanium-sapphire laser is sent on the FPE cavity after a double pass in an acousto-optic modulator (labelled AOM2 in Fig. 2). The frequency of this AOM

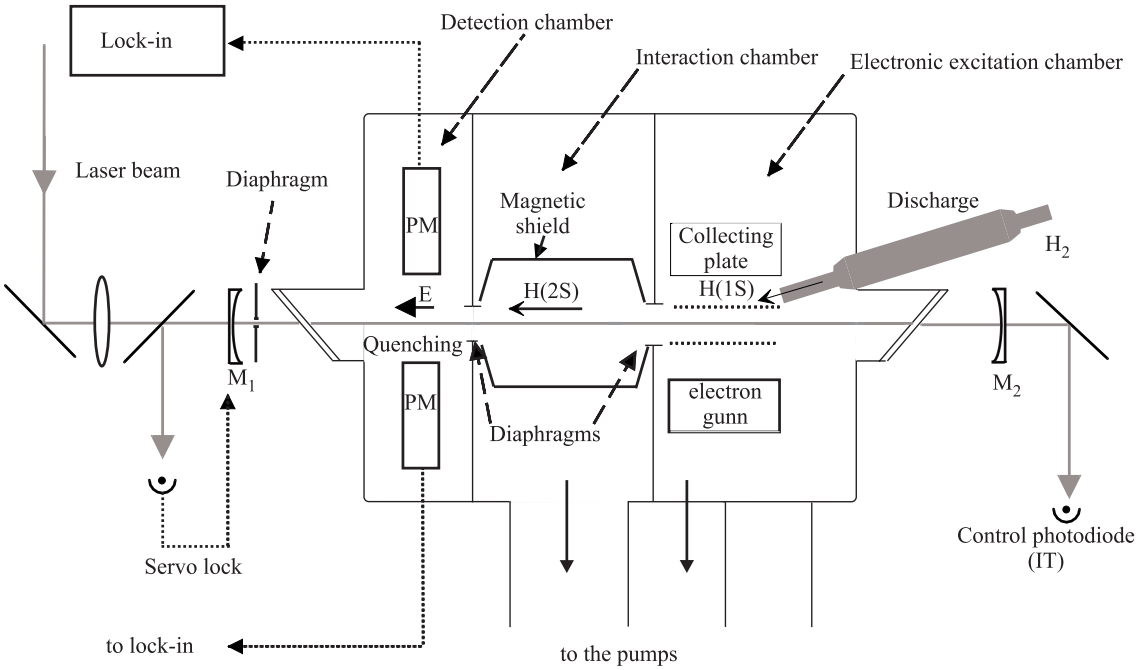

Fig. 4. The metastable hydrogen atomic beam. The three vacuum chambers are not sketched with the same scale: following the laser beams axis, the sizes of the electronic excitation chamber, interaction chamber and detection chamber are respectively 10 cm, 56 cm and 7 cm. M1 and M2: mirrors of the enhancement cavity, PM: photomultiplier.

is locked in order that the transmitted beam is in resonance with the FPE cavity. By this way, we can know the frequencies of the fringes of the FPE cavity with respect to the ones of the FPR cavity. As the free spectral range of the two cavities are slightly different (299.590 MHz and 299.700 MHz for the FPR and FPE cavity respectively), there is a Vernier effect between the two cavities: the relative positions of the fringes of the two cavities are similar every about 2700 fringes (*i.e.* 1.6 nm in terms of wavelength) and, from these measurements, we can deduce the numbers of the fringes of the FPR and FPE cavities with a typical uncertainty of one fringe.

2.3 The metastable hydrogen atomic beam

2.3.1 The atomic beam apparatus

Our metastable atomic beam is sketched in Figure 4. It is very similar to a first apparatus described in reference [16]. The metastable atomic beam is produced in two steps: molecular hydrogen is dissociated in a water cooled Pyrex tube by a radiofrequency discharge (about 26 MHz). An atomic beam flows through a Teflon nozzle and effuses into a first vacuum chamber, which is evacuated by an oil diffusion pump (Alcatel 6250, pumping speed of 2 500 l/s) to a pressure of about 10^{-4} mbar. Thereafter ground state atoms are excited to the 2S metastable state by electronic bombardment (in an equipotential region to prevent the quenching of the metastable atoms, see details in Ref. [16]). The optical excitation takes place in the second vacuum chamber, where the metastable atomic beam is delimited by two holes, 7 mm in diameter, 56 cm apart (this metastable atomic beam makes an angle of 20° with the 1S atomic beam). To evacuate this chamber, we use a cryogenic pump (CTI-Cryogenics CT8, pumping speed of 2 000 l/s for hydrogen) and the running pressure is typically 10^{-6} mbar. In our first experiments [4,5,9], the ambient magnetic field was reduced to less than 20 mG by three pairs of coils. More recently [6,8], we have placed a magnetic shield in the second vacuum chamber (see Fig. 4). To reduce the stray electric fields, the walls of the chamber and the magnetic shield are painted with Aquadag, a conductive colloidal graphite suspension in an ammonia solution. This chamber is also permanently heated to 330 K to prevent the formation of any insulating deposits on the walls and the magnetic shield. From the line shape analysis of the 2S–nD transitions (n in the range 15–20), which are very sensitive to the stray electric fields, we have deduced that this painting reduces the stray electric fields from several tens of millivolts per centimetre to about 3 mV/cm (see Sect. 3). To preserve this property, the Aquadag paint is renewed approximatively about once a year. The metastable atoms are detected in the third vacuum chamber, which is simply evacuated through the 7 mm hole between the two vacuum chambers. An applied electric field quenches the 2S state and two photomultipliers (Hamamatsu R1459) detect the Lyman-α fluorescence. The two photomultiplier windows are 1 cm apart around the quenching region, and the detection solid angle is: $\Omega/4\pi \simeq 60\%$. To detect the photomultiplier signal, the quenching voltage is square-wave modulated at about 1.45 kHz and we use a lock-in amplifier (ATNE ADS2). From the photomultiplier current, we estimate the

metastable beam intensity to be at best 2×10^7 atoms/s (4×10^7 for deuterium). Nevertheless, we work usually with a metastable yield of about 8×10^6 atoms/s, regime where the signal-to-noise ratio is better.

To maximise the excitation rate for the 2S–nS/D two-photon transitions, the whole metastable atomic beam is placed inside an enhancement cavity whose optical axis is in coincidence with the atomic beam. This cavity is formed by two mirrors, 101 cm apart, one flat (high reflector) and the other concave (4 m curvature radius, transmission of about 1.1%). With this geometry, the beam waist is about 660 μm. To reduce the perturbations due to the vibrations of the cryogenic pump, this cavity is mounted on a small granite bench ($220\times20\times13$ cm^3) which is carefully isolated from the vacuum apparatus. The two mirrors are mounted on piezoelectric transducers and the length of the cavity is locked to the laser wavelength by monitoring the reflected beam polarisation [17]. In this servo-loop, the rapid length fluctuations are corrected by a small PZT acting on the flat mirror, which is of a small size (8 mm in diameter, 4 mm thick). Inside the cavity, the optical power can be as much as 100 W in each direction. This light intensity is controlled with a photodiode which measures the small intensity transmitted by the high reflector.

2.3.2 Velocity distribution of the metastable atoms

A precise knowledge of the velocity distribution of the atoms is necessary to calculate the line shapes of the two-photon lines and to deduce the corrections due to the second order Doppler effect. We have measured this velocity distribution by observing the Doppler broadened 2S–6P transition at 410 nm with a collinear laser beam. This laser source is obtained from the titanium-sapphire laser by a frequency doubling in an LBO crystal (see Ref. [13] and Sect. 5). For this measurement, we remove the concave mirror of the enhancement cavity. The beam at 410 nm (typical power of 100 mW) is sent along the metastable beam and a fraction of the laser beam (about 30%) is reflected by the flat mirror of the enhancement cavity, so that the atoms see two counterpropagating waves. Usually, the measurements are made with two different beam waists, one matched to the diameter of the metastable beam (7 mm), the other more focused (about 2 mm) and we have observed that the results are not sensitive to the beam waist. For the detection, the quenching voltage in the third vacuum chamber is applied continuously and the laser beam is chopped at about 120 Hz. At this frequency, the duration of the square-modulation of the light (4 ms) is long with respect to the atomic transit time through the second vacuum chamber (190 μs for an atom at 3 km/s), so that only the very slow atoms (velocity of about 70 m/s) are not detected with this method. The laser frequency is scanned by locking the titanium-sapphire on the successive fringes of the FPR cavity. A typical recording is shown in Figure 5. The signal is split into two peaks, separated by 19 GHz, which are due to the two counterpropagating waves at 410 nm. In a first rough analysis, this separation $\Delta\nu$ corresponds to a beam velocity $c\Delta\nu/2\nu_0$ of

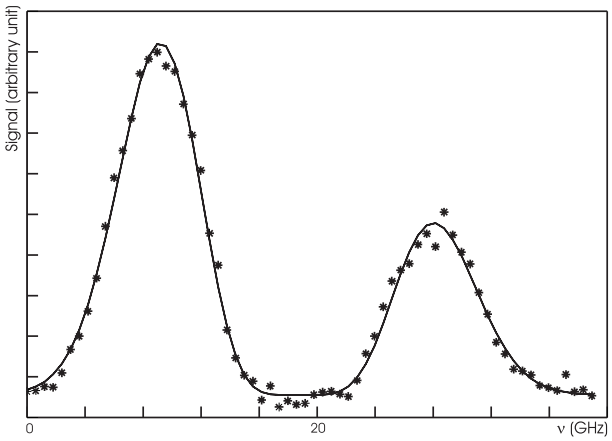

Fig. 5. Doppler broadened profile of the 2S–6P transition at 410 nm (the frequency is two times the frequency of the titanium-sapphire laser at 820 nm).

3.9 km/s (c is the velocity of light and ν_0 the frequency of the 2S–6P transition). The maximum signal is about 10% of the total metastable yield. Because of the long interaction time between the atom and the laser beam, there is a large saturation and the velocity classes are broadened to about 360 MHz, when the natural width of the 6P level is 3.9 MHz.

Due to the electronic excitation of the metastable atoms, the velocity distribution $f(v)$ in the beam should vary as $v^4 \exp(-v^2/2\sigma^2)$, where σ is related to the mass M of the atom and the temperature as $\sigma = \sqrt{kT/M}$[16]. In our case, we have observed that the velocity distribution can be more narrow and we have fitted the data with a velocity distribution of the form:

$$f(v) \sim v^n \exp(-v^2/2\sigma^2) \tag{1}$$

where n is an integer which can be different from 4. With this distribution, the second order Doppler shift $\delta_{\rm D}$ of a transition of frequency $\nu_{\rm trans}$ is, in a simple model (see Ref. [11]):

$$\delta_{\rm D} = -\frac{n}{2}\left(\frac{\sigma}{c}\right)^2 \nu_{\rm trans}. \tag{2}$$

In our first papers [4,5,9], we used simply the equation (2) to determine the second order Doppler shift. In our more recent work [6,8], the velocity distribution is directly included in the line shape calculation of the 2S–nS/D transitions (see Sect. 3).

If we suppose that the light intensity is uniform along an atomic trajectory, the shape $F(\nu)$ of the Doppler broadened 2S–6P line is:

$$F(\nu) \sim \int_0^\infty f(v) H(v,\nu) \mathrm{d}v \tag{3}$$

$$H(v,\nu) = 1 - \exp\left\{-\frac{1}{v}\left[I_+ L\left(\nu - \nu_0\left(1 + v/c\right)\right) + I_- L\left(\nu - \nu_0\left(1 - v/c\right)\right)\right]\right\} \tag{4}$$

Table 1. Velocity distribution of the hydrogen and deuterium atomic beam.

date	n	σ (m/s)	v_{Max} (m/s)	$\delta_{2\mathrm{S}-8\mathrm{D}}$ (kHz)
hydrogen				
1988 [11,16]	4	1525 (10)	3050 (20)	−39.9 (1.0)
1992 [4]	5	1385 (30)	3100 (70)	−41.0 (2.0)
1993 [5]	5	1406 (33)	3144 (75)	−42.4 (2.0)
1996 [6]	5	1814 (13)	4056 (29)	−70.6 (1.0)
1997 [8]	6	1614 (11)	3953 (27)	−67.0 (1.0)
deuterium				
1988 [11,16]	4	983 (10)	1966 (20)	−16.6 (1.0)
1997 [6]	7	995 (10)	2633 (26)	−29.7 (1.0)
1998 [8]	6	1044 (10)	2557 (24)	−26.3 (1.0)

where I_+ and I_- are proportional to the intensity of the two travelling waves and $L(\nu)$ is the Lorentzian profile of the 2S–6P transition. In this equation, we have neglected the fine and the hyperfine structures of the 2S and 6P levels (the largest is the 6P fine structure $\Delta\nu_0 \sim 400$ MHz). A simple model shows that this approximation leads to, for the second order Doppler shift, a relative error of $(\Delta\nu_0/\Delta\nu)^2 \simeq 5\times10^{-4}$ (*i.e.* an error of about 40 Hz for the frequencies of the 2S–nS/D transitions). The function $H(v,\nu)$ describes the two velocity classes which are excited by the two travelling waves. Because of the saturation of 2S–6P transition, the width of these velocity classes varies as $1/\sqrt{v}$. Consequently the function $H(v,\nu)$ can be approximated by two square functions of v at the velocities $v_0 = \pm c(\nu-\nu_0)/\nu_0$, with a height of unity and a width proportional to $1/\sqrt{|v_0|}$. With these approximations, the shape $F(\nu)$ becomes:

$$F(\nu) = A(\nu-\nu_0)^{n-1/2}\exp\left[-(\nu-\nu_0)^2/2\sigma_\nu^2\right] \quad \text{if} \quad \nu>\nu_0 \quad (5)$$

$$F(\nu) = B(\nu_0-\nu)^{n-1/2}\exp\left[-(\nu-\nu_0)^2/2\sigma_\nu^2\right] \quad \text{if} \quad \nu<\nu_0 \quad (6)$$

where A and B are two adjustable constants and $\sigma_\nu = \nu_0\sigma/c$. From the fit of the profile $F(\nu)$ to the experimental data, we deduce the integer n and the parameter σ which describe the velocity distribution.

The results for the measurements made since 1988 are given in Table 1 where we also show the most probable velocity $v_{\mathrm{Max}} = \sqrt{n}\sigma$ and the second order Doppler shift $\delta_{2\mathrm{S}-8\mathrm{D}}$ of the 2S–8D transition (Eq. (2)). We can make two comments: (i) during the period 1988–1993, the typical velocity of the hydrogen beam was very stable, v_{Max} being around 3.1 km/s. By contrast, in the experiments made since 1996, the atoms have been distinctly more rapid, with a velocity of about 4 km/s. This velocity increase appeared after an accidental contamination of the vacuum apparatus by the oil of the diffusion pump. After this pollution, the beam velocity was less reproducible and, in spite of our careful cleaning of the vacuum system, we have never been able to obtain the original characteristics of the atomic beam. This effect is probably due to the destruction of the slow atoms by the stray electric fields which are more important in the first vacuum chamber since this contamination. (ii) On the other hand, the ratio between the hydrogen and deuterium velocities is very stable with a value of 1.55. This value is slightly different from the $\sqrt{2}$ factor to be expected for a thermal beam. This fact can be explained by the deviation due to the electronic excitation of the 2S level. For deuterium, the mean deviation is only 14° and the 20° angle of our atomic beam apparatus selects the slow deuterium atoms.

2.4 Data acquisition

The experiment is driven by a microcomputer which commands the frequency of the titanium-sapphire laser (through the synthesizer which drives the AOM1), performs the acquisition of the atomic signal and records several other parameters of the experiment: the signal of the photodiode which monitors the light intensity inside the enhancement cavity, the frequency of the beat note between the two He–Ne lasers, the modulation frequency of the AOM2 and several other frequency measurements used to determine the optical frequency of the laser (see Sect. 4). The atomic spectrum is divided in 101 frequency points. For each point, the duration of the measurement is 1 s (the signal of the lock-in amplifier which detects the atomic signal is acquired 10 times every 100 ms with a time constant of 100 ms) and there is a dead time of about 300 ms for the acquisition procedure by the computer and the shift of the laser frequency. To reduce the effect of the low drift of the metastable yield, the sweep of the line is not regular: the 101 points are obtained by 10 scans of the line in the following order:

0	10	20	30...80	90	100
99	89	79	69...19	9	
8	18	28	38...88	98	
...					
91	81	71	61...11	1	

Finally, the laser frequency is scanned ten times across the atomic resonance during a 22 minutes run. After an average of these 10 scans, the relative noise of the metastable yield is about 0.3%.

Figure 6 shows a typical signal obtained in the case of the $2S_{1/2}(F=1)$–$8D_{5/2}$ transition of hydrogen. In this recording, the decrease of the metastable intensity is 13% and the linewidth 1.13 MHz (in terms of atomic frequency). By comparison with the natural width of the 8D level (572 kHz), there is a large broadening which is mainly due to the inhomogeneous light shift experienced by the atoms through the Gaussian profile of the laser beams. To evaluate this effect, we record the signal for several laser intensities and we made an extrapolation

Table 2. Some features of the observed transitions.

transition	number of runs	amplitude of a scan	width variation	maximum amplitude
hydrogen				
$2S_{1/2}(F=1)$–$6D_{5/2}$ [9]	49	10 MHz	1.8 MHz to 3.4 MHz	19.7%
$2S_{1/2}(F=1)$–$6S_{1/2}$ [9]	91	4 MHz	400 kHz to 1.2 MHz	5.7%
$2S_{1/2}(F=1)$–$8D_{5/2}$ [5]	20	8 MHz	900 kHz to 2.1 MHz	18.6%
$2S_{1/2}(F=1)$–$8D_{3/2}$ [5]	24	8 MHz	900 kHz to 1.9 MHz	16.0%
$2S_{1/2}(F=1)$–$8S_{1/2}$ [5]	47	4 MHz	330 kHz to 800 kHz	5.1%
$2S_{1/2}(F=1)$–$8D_{5/2}$ [6]	90	8 or 12 MHz	750 kHz to 2.0 MHz	21.7%
$2S_{1/2}(F=1)$–$8D_{3/2}$ [6]	53	8 or 12 MHz	800 kHz to 1.6 MHz	18.5%
$2S_{1/2}(F=1)$–$8S_{1/2}$ [6]	77	2.8 or 4 MHz	300 kHz to 950 kHz	6.7%
$2S_{1/2}(F=1)$–$12D_{5/2}$ [8]	78	3.6 MHz	300 kHz to 600 kHz	8.7%
$2S_{1/2}(F=1)$–$12D_{3/2}$ [8]	62	3.6 MHz	300 kHz to 600 kHz	6.7%
deuterium				
$2S_{1/2}(F=3/2)$–$8D_{5/2}$ [6]	41	8 or 12 MHz	750 kHz to 2.2 MHz	19.8%
$2S_{1/2}(F=3/2)$–$8D_{3/2}$ [6]	49	8 or 12 MHz	700 kHz to 2.0 MHz	19.5%
$2S_{1/2}(F=3/2)$–$8S_{1/2}$ [6]	47	2.8 or 4 MHz	250 kHz to 1.0 MHz	7.3%
$2S_{1/2}(F=3/2)$–$12D_{5/2}$ [8]	44	3.6 MHz	300 kHz to 650 kHz	9.1%
$2S_{1/2}(F=3/2)$–$12D_{3/2}$ [8]	54	3.2 MHz	350 kHz to 650 kHz	8.3%

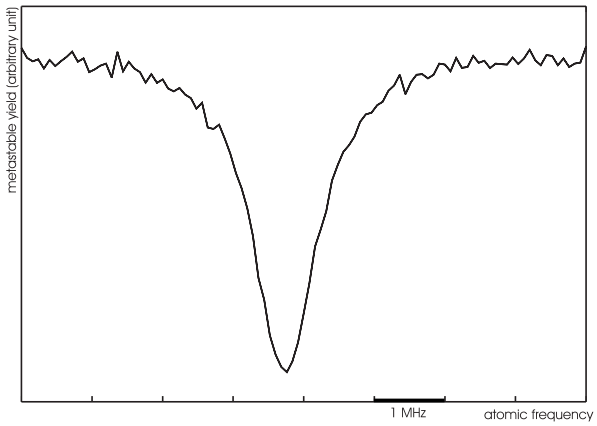

Fig. 6. Typical two-photon transition signal, recorded as a decrease of the metastable beam intensity. Example of the $2S_{1/2}(F=1)$–$8D_{5/2}$ transition of hydrogen: the decrease of the metastable yield is 13%.

to zero light power. Consequently, the data acquisition takes 3 or 4 days for each atomic transition. Table 2 gives some details for the measurements which have been made during the period 1993–1998 [5,6,8,9]. For each transition, we indicate the number of the runs used for the extrapolation, the amplitude of the frequency scan (in terms of atomic frequency), the range of variation of the line width with the light power and the maximum amplitude of the observed signal.

3 Line shape analysis

3.1 Expression for the line shape

Figure 7 shows an atomic trajectory in the laser-atom interaction region (the second vacuum chamber). In this region, the collisions are negligible and the atomic trajectories are straight lines passing through the two diaphragms (the small deviation of the atomic trajectory due to the forces induced by the light shifts will be studied below). The calculation procedure is the following. In a first step, we calculate for each trajectory the destruction probability of the metastable atom when it crosses the laser beam. Then we make an average over all the possible trajectories.

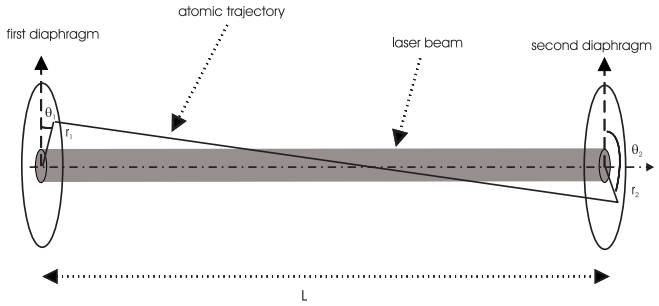

Fig. 7. Schematic view of an atom trajectory in the laser-atom interaction region.

3.1.1 Two-photon excitation rate

The two-photon transition probability Γ_g between two states $|g\rangle$ and $|e\rangle$ (energies E_g and E_e) is given by [11,18]:

$$\Gamma_g = \frac{n^2\omega^2}{\varepsilon_0^2\hbar^2}\left|\sum_r \frac{\langle e|\,\mathbf{d}\cdot\varepsilon\,|r\rangle\,\langle r|\,\mathbf{d}\cdot\varepsilon\,|g\rangle}{\omega-\omega_{rg}}\right|^2 \times \frac{\Gamma_e}{(2\omega-\omega_{eg})^2+(\Gamma_e/2)^2} \quad (7)$$

$$\Gamma_g = \left(\frac{4\pi a_0^2}{mc^2\alpha}\right)^2 \sum_e \frac{\left|\langle e\left|Q_{\rm tp}\right|g\rangle\right|^2 \Gamma_e \left(1+c_{\rm io}I\right) I^2}{\left[2\omega - \left(\omega_{eg}\left(1-v^2/c^2\right)+c_{\rm ls}I\right)\right]^2 + \left[\Gamma_e\left(1+c_{\rm io}I\right)/2\right]^2 \left(1+c_{\rm sat}I^2\right)} \tag{10}$$

Table 3. 2S–nS/D two-photon transition amplitude $\langle e\left|Q_{\rm tp}\right|g\rangle$ and natural width of the excited level.

transitions	$\langle e\left\|Q_{\rm tp}\right\|g\rangle$ (a.u.)	$\Gamma_e/2\pi$
2S–6S	−14.711	297 kHz
2S–8S	−14.921	144 kHz
2S–6D	−133.16	1.337 MHz
2S–8D	−92.937	572 kHz
2S–12D	−55.033	172 kHz
2S–15D	−40.677	88.7 kHz
2S–20D	−27.187	19.0 kHz

where n is the number of photons per unit volume for each counterpropagating wave, ω the laser frequency, ε the polarisation, $\omega_{ij} = (E_i - E_j)/\hbar$, $\mathbf{d}$ the electric dipole moment operator and Γ_e the natural width of the excited state (we suppose that the natural width of the state $|g\rangle$ is negligible). The summation is made over all the possible states $|r\rangle$ (including the continuum). We introduce the two-photon operator $Q_{\rm tp}$. In our experiment, the polarisation of the laser beam is linear (because of the Brewster windows of the vacuum apparatus placed in the enhancement cavity). For a polarisation along the z-axis, $Q_{\rm tp}$ is given in atomic units ($\hbar = \alpha c = m = 1$) by:

$$Q_{\rm tp} = \sum_r \frac{z\left|r\right\rangle\left\langle r\right|z}{\omega - \omega_{rg}}\,. \tag{8}$$

With this notation, equation (7) becomes:

$$\Gamma_g = \left(\frac{4\pi a_0^2}{mc^2\alpha}\right)^2 \frac{\left|\langle e\left|Q_{\rm tp}\right|g\rangle\right|^2 \Gamma_e I^2}{\left(2\omega-\omega_{eg}\right)^2 + \left(\Gamma_e/2\right)^2} \tag{9}$$

where I is the power density of the light ($I = n\hbar\omega/c$), a_0 the Bohr radius, α the fine structure constant and m the electron mass. For the transitions studied in this paper, Table 3 gives the values of the matrix element $\langle e\left|Q_{\rm tp}\right|g\rangle$ (calculated in Ref. [11]) for an atom without electronic and nuclear spin, and the natural width of the excited level.

In the calculation of the line shape of the 2S–nS/D transitions, we have taken into account the fine and hyperfine structures of the S and D levels, the light shift, the second order Doppler effect, the photoionisation of the upper level and the saturation of the two-photon transition. The states $|g\rangle$ and $|e\rangle$ are the magnetic hyperfine sublevels $|F_g m_F\rangle$ and $|F_e m_F\rangle$ (F_i is the total angular momentum of the state $|i\rangle$, $|i\rangle = |g\rangle$ or $|e\rangle$). We have the selection rule $\Delta m_F = 0$. Then the two-photon transition probability becomes:

see equation (10) above.

The coefficients $c_{\rm ls}$, $c_{\rm io}$ and $c_{\rm sat}$ describe the light shift, the photoionisation, and the saturation of the two-photon transition.

Following the notations of reference [11], the light shift coefficient is given by:

$$c_{\rm ls} = \left(\frac{4\pi a_0^2}{mc^2\alpha}\right)\left(\beta_e - \beta_g\right)$$

where β_i are the matrix elements of the light shift operator $Q_{\rm ls}$. We have:

$$Q_{\rm ls} = \sum_r \left[\frac{z\left|r\right\rangle\left\langle r\right|z}{\omega_{ir}+\omega} + \frac{z\left|r\right\rangle\left\langle r\right|z}{\omega_{ir}-\omega}\right] \qquad \text{(atomic units)}. \tag{11}$$

The light shift operator is the sum of a scalar operator $Q_{\rm ls}^0$ and of an operator of rank 2 $Q_{\rm ls}^2$. For the state $|i\rangle = |nLJFm_F\rangle$ (n principal quantum number, L and J orbital and electronic momenta), straightforward algebra gives:

$$\begin{aligned}\langle i\left|Q_{\rm ls}\right|i\rangle = {} & \frac{\langle nL\left\|Q_{\rm ls}^0\right\|nL\rangle}{\sqrt{2L+1}} \\ & + (-1)^{F-m_F}\begin{pmatrix} F & 2 & F \\ -m_F & 0 & m_F\end{pmatrix}\langle JF\left\|Q_{\rm ls}^2\right\|JF\rangle\end{aligned} \tag{12}$$

where:

$$\begin{aligned}\langle JF\left\|Q_{\rm ls}^2\right\|JF\rangle = {} & (-1)^{F+I+2J+L+S}\left(2F+1\right)\left(2J+1\right) \\ & \times \begin{Bmatrix} J & 2 & J \\ F & I & F\end{Bmatrix}\begin{Bmatrix} L & 2 & L \\ J & S & J\end{Bmatrix}\langle nL\left\|Q_{\rm ls}^2\right\|nL\rangle.\end{aligned}$$

The calculation of the matrix elements $\langle nL\left\|Q_{\rm ls}^k\right\|nL\rangle$ and ionisation coefficient $c_{\rm io}$ has been made with a method using Sturmian functions [19] (the coefficient $c_{\rm io}$ can be also obtained with the Fermi's golden rule, see Refs. [11,20, 21]). Table 4 gives the values of these parameters. The effect of the ionisation is not entirely negligible. For example, for a laser beam of 100 W with a waist of 660 μm, the ionisation rate of the 8S level is, at the center of the beam, 1.5×10^5 s^{-1}, *i.e.*, because of this ionisation probability, the width of the 8S level increases by 24 kHz. The saturation coefficient $c_{\rm sat}$ can be obtained by using an effective Hamiltonian [22]. Its expression is:

$$c_{\rm sat} = 8\left(\frac{4\pi a_0^2}{mc^2\alpha}\right)^2 \frac{\left|\langle e\left|Q_{\rm tp}\right|g\rangle\right|^2}{\Gamma_e^2}\,. \tag{13}$$

Table 4. Light shift and ionisation coefficients for the 2S–nS or 2S–nD transitions studied in this paper (expressed in atomic units).

transitions	$\langle nL_g \left\|\|Q^0_{\rm ls}\right\|\| nL_g\rangle$ (a.u.)	$\langle nL_e \left\|\|Q^0_{\rm ls}\right\|\| nL_e\rangle$ (a.u.)	$\langle nL_e \left\|\|Q^2_{\rm ls}\right\|\| nL_e\rangle$ (a.u.)	ionisation coefficient $c_{\rm io}$ ($\rm m^2W^{-1}$)
2S–6S	−290.96	324.42	0	1.536×10^{-9}
2S–8S	−355.31	291.35	0	1.144×10^{-9}
2S–6D	−290.96	727.20	34.99	2.315×10^{-10}
2S–8D	−355.31	648.51	19.19	1.805×10^{-10}
2S–12D	−428.53	603.94	6.78	1.517×10^{-10}

Table 5. Data for the calculation of the $2S(F=1)$–$8D_{5/2}$ two-photon line shape.

transition	F_e	hyperfine shift	$a_{\rm hfs}$ weight of the F_e level	$\beta_{\rm 2S}$ (a.u.)	β_{F_e} (a.u.)
hydrogen					
$2S_{1/2}(F=1)$–$8D_{5/2}$	2	−82.3 kHz	2/9	−355.31	288.19
	3	59.4 kHz	7/9	−355.31	286.88
deuterium					
$2S_{1/2}(F=3/2)$–$8D_{5/2}$	3/2	−25.6 kHz	1/15	−355.31	290.02
	5/2	−7.3 kHz	4/15	−355.31	289.16
	7/2	18.3 kHz	2/3	−355.31	287.22

This effect is also not negligible: with the same laser beam parameters as above, the value of $c_{\rm sat}I^2$ is about 0.1 for the $2S_{1/2}$–$8D_{5/2}$ transition.

In the case of the 2S–nS transition, the two-photon operator is scalar and we have the selection rules $\Delta F = 0$, $\Delta m_F = 0$. In equation (10) the summation over the states $|e\rangle$ is reduced to a single term and, for the two-photon matrix element, we have $\langle nL_eJ_eFm_F|\, Q_{\rm tp}\, |2L_gJ_gFm_F\rangle = \langle nL_em_L|\, Q_{\rm tp}\, |2L_gm_L\rangle$. For the 2S–$n$D transition, the two-photon operator is quadrupolar and, in equation (10), we have to make the sum, for each m_F value, on all the states $|F_em_F\rangle$. Nevertheless, as the quadrupolar term of the light shift is very small (see Tab. 4), we have used the mean values (with respect to the magnetic quantum number m_F) of the light shift coefficient $c_{\rm ls}$ (given by Eq. (12)) and of the intensities of the hyperfine components. With these approximations, the two-photon transition probability Γ_g does not depend on m_F. The summation in equation (10) is made over the F_e quantum number and the two-photon fine and hyperfine intensities are given by:

$$|\langle nL_eJ_eFm_F|\, Q_{\rm tp}\, |2L_gJ_gFm_F\rangle|^2 = a_{\rm fs}a_{\rm hfs}\, |\langle nL_em_L|\, Q_{\rm tp}\, |2L_gm_L\rangle|^2 . \quad (14)$$

The matrix elements $\langle nL_em_L|\, Q_{\rm tp}\, |2L_gm_L\rangle$ have been given in Table 3. The coefficient $a_{\rm fs}$ takes into account the fine structure of the D level. It is proportional to the degeneracy $2J_e + 1$ (0.4 and 0.6 for the $D_{3/2}$ and $D_{5/2}$ levels). The coefficient $a_{\rm hfs}$ describes the intensity of the hyperfine components and is proportional to [12]:

$$(2F_e+1)\left\{\begin{array}{ccc} J_e & J_g & 2 \\ F_g & F_e & I \end{array}\right\}^2 .$$

As an example, Table 5 gives the numerical values used in equation (10) for the $2S(F=1)$–$8D_{5/2}$ transition. The hyperfine splittings are calculated with the Fermi's formula [20].

3.1.2 Destruction probability of the metastable atoms

We consider an atomic trajectory between two points (r_1, θ_1) and (r_2, θ_2) on the diaphragms which delimit the metastable beam (see Fig. 7). If the laser beam is aligned with the x-axis, the laser intensity varies along the atomic trajectory as:

$$I(x,\rho) = I_0 \left(\frac{w_0}{w(x)}\right)^2 \exp\left[-2\left(\frac{\rho}{w(x)}\right)^2\right] \quad (15)$$

where x is the coordinate along the laser beam, ρ the radial distance to the laser beam axis, $w(x)$ the radius of the laser beam. Along the atomic trajectory, ρ is a function $\rho(x)$ and, if we assume that the transit time of the atom through the laser beam is long with respect to the life time $1/\Gamma_e$ of the excited level, the two-photon transition probability Γ_g becomes a function of x. The probability that the atom undergoes a transition during this trajectory is:

$$P(r_1,\theta_1,r_2,\theta_2) = 1 - \exp - \int_0^L \frac{\Gamma_g(x)\mathrm{d}x}{v_x} \quad (16)$$

Table 6. Two-photon cascade probability R_n from the nS or nD levels to the 2S metastable state.

level	6S	6D	8S	8D	12D	15D	20D
R_n	0.0740	0.0463	0.0815	0.0513	0.0548	0.0558	0.0567

Table 7. Partition of the probability R_n between the two hyperfine levels of the metastable state when the two-photon excitation is made from the $2S_{1/2}(F = 1)$ hyperfine sublevel ($F = 3/2$ for deuterium).

upper level	$nS_{1/2}$	$nD_{3/2}$	$nD_{5/2}$
hydrogen			
p_0	$(4/27)R_n$	$(32/135)R_n$	$(2/15)R_n$
p_1	$(23/27)R_n$	$(103/135)R_n$	$(13/15)R_n$
deuterium			
$p_{1/2}$	$(16/81)R_n$	$(128/405)R_n$	$(8/45)R_n$
$p_{3/2}$	$(65/81)R_n$	$(277/405)R_n$	$(37/45)R_n$

where v_x is the component of the atom velocity along the x axis and L the distance between the two diaphragms. We have to correct this expression to take into account the hyperfine structure and the repopulation of the 2S level.

(i) *Hyperfine structure of the metastable state.* In our experiment, we resolve the hyperfine structure of the metastable state and we have studied the most intense transitions starting from the $2S_{1/2}(F = 1)$ hyperfine level ($2S_{1/2}(F = 3/2)$ for deuterium). As we detect all the metastable atoms we have to multiply the equation (16) by a coefficient $C_{\rm hfs}$ which describes the population of the two hyperfine levels. By observing some transitions starting from the $2S_{1/2}(F = 0)$ hyperfine level ($2S_{1/2}(F = 1/2)$ for deuterium), we have measured these populations:

$$C_{\rm hfs}(F = 1) = 80\% \qquad \text{in hydrogen,}$$

$$C_{\rm hfs}(F = 3/2) = 67.6\% \qquad \text{in deuterium.}$$

These values are slightly different from the statistical weights (3/4 and 2/3 respectively). This effect is probably due to a larger quenching of the $2S_{1/2}(F = 0)$ ($2S_{1/2}(F = 1/2)$ in deuterium) which is closer to the $2P_{1/2}$ level and more sensitive to the stray electric fields.

(ii) *Repopulation of the metastable state.* When an atom is excited to the nS or nD level, it can undergo a radiative cascade towards the $2S_{1/2}$ level with the probability $R_n = p_0 + p_1$ ($p_{1/2} + p_{3/2}$ for deuterium), where the probabilities p_0 and p_1 ($p_{1/2}$ and $p_{3/2}$ for deuterium) are correlated to the two $2S_{1/2}(F = 0)$ and $2S_{1/2}(F = 1)$ levels (respectively $F = 1/2$ and $F = 3/2$ for deuterium). These probabilities have been calculated taking into account only the two photon cascades [11]. The values relevant to this paper are given in Tables 6 and 7.

Finally, after solving the rate equations which describe the evolution of the populations of the two hyperfine sublevels, we obtain the destruction probability of a metastable atom at the end of its trajectory:

$$P'(r_1, \theta_1, r_2, \theta_2) = C_{\rm hfs}\left(1 - \frac{p_0}{1 - p_1}\right) \times \left[1 - \exp -\frac{1}{v_x}\int_0^L (1 - p_1)\, \Gamma_g(x) {\rm d}x\right]. \quad (17)$$

For deuterium, we have to replace in equation (17) the probabilities p_0 and p_1 by $p_{1/2}$ and $p_{3/2}$. The first factor describes the optical pumping from the $F = 1$ hyperfine sublevel to the $F = 0$ one. The factor $1 - p_1$ in the integral describes the inefficiency of the two-photon excitation when the atom comes back to the initial $F = 1$ hyperfine sublevel.

Up to now, we have supposed that the atomic trajectories were straight lines. Let us consider the effect of the force due to the light shift of the metastable state. As the 2S state is down shifted (see Tab. 4), the atom is attracted towards the axis of the laser beam by a force $F_\rho(x, \rho)$ (we neglect the component of this force along the x-axis):

$$F_\rho(x, \rho) = -\hbar\beta_g \left(\frac{4\pi a_0^2}{mc^2\alpha}\right) \frac{\partial}{\partial\rho} I(x, \rho).$$

The acceleration due to this force is considerable. For example, for a laser beam of 100 W with a waist of 660 μm, the maximum radial acceleration is about 350 m/s^2. Nevertheless, because of the small transit time of the atom through the second vacuum chamber (typically 190 μs), the deviation from a straight trajectory is small, about a few micrometres. Even so, in the case of the 2S–nD transitions, which give the most accurate results, we have included this effect for the line shape calculation. The atomic trajectory is calculated step by step to determine the function $\rho(x)$ which is used to obtain the intensity $I(x, \rho)$ (Eq. (15)) and the two-photon transition probability $\Gamma_g(x)$ (Eq. (10)).

3.1.3 Summation on the atomic trajectories and velocities

The last step of this calculation is to make a summation of equation (17) over all velocities and all possible trajectories. We have studied the velocity distribution $f(v)$ in Section 2 and these functions are given in Table 1. On the other hand, we do not know the exact distribution of the atomic trajectories. Because of the recoil of the atom involved by the electronic excitation of the 2S state, there is a large dispersion in the direction of the metastable atoms. For this reason, we can suppose a uniform distribution for the points (r_2, θ_2) at the end of the atomic beam. This is not the case however at the beginning of the beam. The distribution of the metastable atoms can depend on the

spatial distribution of the 1S hydrogen atoms, the electron density or the quenching stray electric fields. Our approach has been to simulate the spatial distribution of the points (r_1, θ_1) by a uniform one on a virtual diaphragm centered on the real diaphragm at the beginning of the beam but with a smaller radius R_1. In this case the line shape $L(\omega)$ is given by:

$$L(\omega) = \frac{4}{\pi R_1^2 R_2^2} \int_0^\infty f(v)\mathrm{d}v \int_0^{R_1} r_1 \mathrm{d}r_1 \int_0^{R_2} r_2 \mathrm{d}r_2 \times \int_0^\pi \mathrm{d}\theta_2 P'(r_1, \theta_1, r_2, \theta_2). \quad (18)$$

We have supposed that we have a cylindrical symmetry and that the laser beam is well aligned with respect to the atomic beam. R_2 is the radius of the real diaphragm at the end of the atomic beam ($R_2 = 3.5$ mm). As explained below, the radius R_1 is determined during the analysis of the experimental curves to obtain a correct evaluation of the light shift. A typical value is $R_1 = 2$ mm.

3.1.4 Other broadening and shifting effects

In the above analysis, we have neglected several other effects which can broaden or shift the line. The Stark effect produced by the stray electric fields, which can induce a significant shift, will be studied subsequently. The other effects are the following.

(i) *Laser line width.* The jitter of our laser is about 2 kHz (see Sect. 2) corresponding to a line broadening of 4 kHz in terms of atomic frequency.

(ii) *Finite transit time.* Though the metastable atomic beam and the laser beam are colinear, the broadening due to the finite transit time of the atoms through the laser beam is not entirely negligible. For an atomic trajectory making an angle θ with the laser beam, the line broadening is $2v \sin\theta\sqrt{\ln 2}/\pi w$ [23]. In the case of the largest possible angle θ (about 0.6°), this broadening is 32 kHz for a velocity of 4 km/s and a waist of 660 μm.

(iii) *Residual magnetic field.* As the atomic beam is placed in a magnetic shield, the residual magnetic field is about 1 mG. For the 2S–nS transitions, the Zeeman splittings of the 2S and nS levels are similar. Because of the selection rules $\Delta F = 0$, $\Delta m_F = 0$, there is no broadening. In the case of the 2S–nD transition, the broadening due to the Zeeman effect can be about 10 kHz, but there is no shift if the laser polarisation is linear.

(iv) *Black body radiation.* The black body radiation induces transitions between the different hydrogen energy levels. Consequently, there is a depopulation of each level of the two-photon transition, *i.e.* a broadening of the line, and a shift. These effects are studied in detail in reference [24] for a temperature of 300 K. In our experiment, the magnetic shield which surrounds the atomic beam is heated at about 330 K.

Table 8. Broadening and shift due to the black body radiation.

transition	broadening	shift
2S–6S	1.2(0.1) kHz	−360(90) Hz
2S–6D	1.7(0.2) kHz	−430(105) Hz
2S–8S	4.4(0.4) kHz	520(130) Hz
2S–8D	5.5(0.5) kHz	650(160) Hz
2S–12D	7.1(0.7) kHz	2.1(0.5) kHz

If we assume an uncertainty of 30 K to take into account the inhomogeneity of the heating, we obtain the broadenings and shifts given in Table 8. Using the data of reference [24], we have supposed that the broadening varies as the temperature T and the shift as $T^{2.7}$.

3.2 Analysis of the data

3.2.1 Fit procedure

The aim of this analysis is to determine very precisely, with respect to our very stable FPR cavity, the transition frequency, corrected for the light shift, the second order Doppler effect and the nD hyperfine structure. As the two-photon transitions are observed by measuring the decrease of the metastable yield, we can calibrate this decrease with respect to the intensity of the metastable beam when the laser is off resonance. The principle of the adjustement procedure is hence the following: from the amplitude of this decrease we deduce the optical power and, consequently, the light shift.

In practice the theoretical curves given by equation (18) are adjusted to fit the experimental data. As the numerical calculations of the theoretical line shape are long (there is a quintuple integration), we calculate a set of theoretical curves for several laser powers P ($P = \pi w_0^2 I_0/2$) from 5 W to 150 W with a step of 5 W, and as a function of 301 atomic frequency points. The frequency steps are adjusted to the line width (50 kHz for the 2S–6D and 2S–8D transitions, 25 kHz for the 2S–12D and 20 kHz for the 2S–6S and 2S–8S). We obtain the curves $L(\omega, P)$. Then we make two convolutions: a first convolution following ω by a Gaussian curve of width Δ_ω which takes into account the broadening effects which are not included in the line shape, and a second convolution following P by an other Gaussian curve of width Δ_P which describes the fluctuations of the light power seen by the atoms. The width Δ_P is deduced, for each recording, from the light intensity measurements obtained using the enhancement cavity by a photodiode. Finally, the four parameters of the adjustment are the metastable yield when the laser is off resonance, the light power P, the frequency of the atomic transition CLP (without the light shift, the second order Doppler effect and the hyperfine structure of the D level) and the Gaussian broadening Δ_ω. During the adjustement, we make an interpolation, quadratically for the power and linearly for the frequencies.

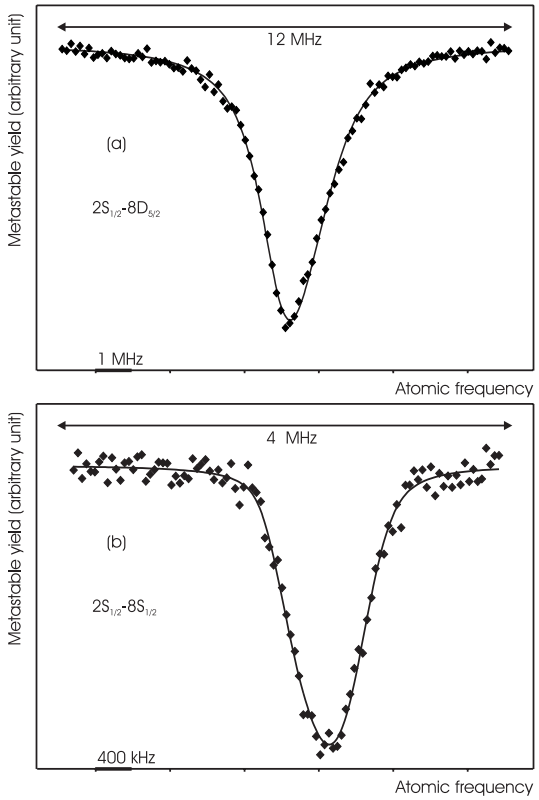

Fig. 8. Fit of the experimental line profile with the theoretical one. (a) $2S_{1/2}(F = 3/2)$–$8D_{5/2}$ transition in deuterium. (b) $2S_{1/2}(F = 3/2)$–$8S_{1/2}(F = 3/2)$ transition in deuterium. The light powers deduced from the fits are respectively 90.6(2.2) W and 96.2(2.6) W and the decreases of the metastable yield 18% and 6%.

Figures 8a and 8b show two examples of adjustements in the case of the $2S_{1/2}$–$8D_{5/2}$ and $2S_{1/2}$–$8S_{1/2}$ transitions of deuterium. The asymmetry of the experimental recordings, which appears for both transitions, but with different signs, is well reproduced by the theoretical profiles. For the $2S_{1/2}$–$8S_{1/2}$ transition, this asymmetry is related to the quadratic dependence with $I(x, \rho)$ of the atomic excitation rate at any point in the beam, since the light shift is linear with $I(x, \rho)$. Thus, the more shifted contributions to the signal are also the more intense. In the case of the $2S_{1/2}$–$8D_{5/2}$ transition, there is a very large saturation of the two-photon excitation probability. This saturation reduces the weight of the more shifted contributions to the signal, so that the sign of the asymmetry is reversed. In both cases, experimental and theoretical profiles are in excellent agreement.

3.2.2 Extrapolation versus the light power

The most crucial point of our analysis is the determination of the optical power seen by the atoms. A first test is to compare the fitted power P with the signal IT given by the photodiode placed after the enhancement cavity (see Fig. 9). There is a good agreement between these

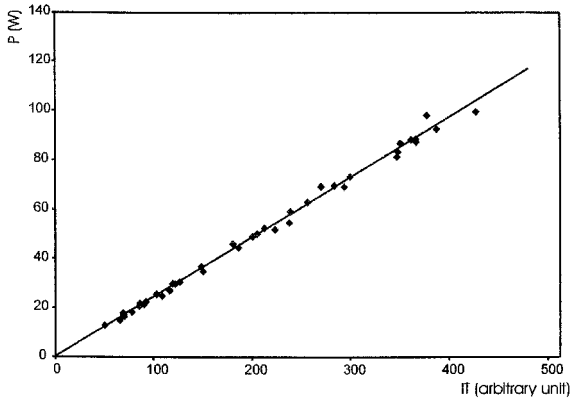

Fig. 9. Fitted power P *versus* the photodiode signal IT for the $2S_{1/2}(F = 3/2)$–$8D_{5/2}$ transition in deuterium (40 recordings).

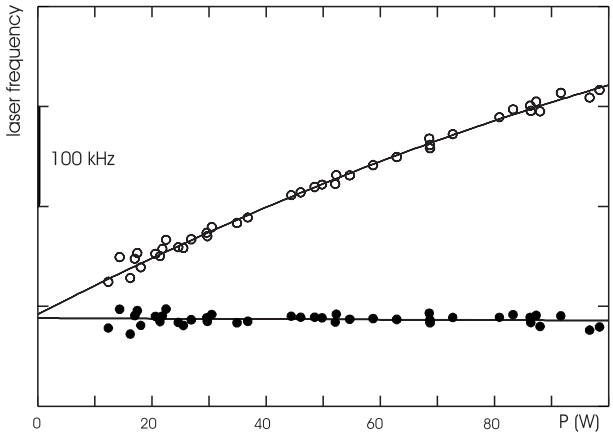

Fig. 10. Extrapolation of the half maximum center (○) and of the line position corrected for the light-shift, second-order Doppler effect and 8D hyperfine structure (●) *versus* the light power P in the case of the $2S_{1/2}(F = 3/2)$–$8D_{5/2}$ transition of deuterium.

data which lie in a linear ratio. We use the slope of this straight line P/IT as a parameter to control the optical alignment of the experiment: the slope P/IT is maximised to obtain the best matching between the laser beams and the atomic beam. The slope P/IT is also determined by the distribution of the atomic trajectories. For example, if we increase the radius R_1 of the first diaphragm, the theoretical curves exhibit a smaller decrease of the metastable yield, and, consequently, the fitting procedure gives a larger light power P. To determine the correct value for R_1, we study the shift of the line position *versus* the laser power. For each record, the adjustment procedure gives us the corrected line position CLP and the half-maximum center of the line HMC. Figure 10 shows a typical extrapolation of the HMC and CLP data *versus* the light power. Because of the saturation of the two-photon transition probability, the variation of HMC is not exactly linear with P. The shift of the line is about 400 kHz for a power of 100 W. On the other hand, there is no variation of the corrected line position. This result has been obtained by varying the radius R_1 to eliminate

Table 9. Calculation of the position of the line in the case of the $2S_{1/2}$–$8D_{3/2}$ transition in hydrogen. The extrapolated values are the absolute frequencies given in terms of laser frequency (*i.e.* $CLP/2$). Here we have indicated only the last digits and the real value is obtained by adding 385 324 GHz.

distribution of the trajectories	$R_1 = 1.8$ mm	$R_1 = 2$ mm
slope of the straight line P/IT (arb. units)	0.224	0.246
extrapolation of CLP *versus* P (MHz)	730.029 80	730.030 72
uncertainty (kHz)	3.27	3.23
extrapolation of CLP *versus* IT (MHz)	730.030 35	730.031 05
uncertainty (kHz)	3.21	3.20
mean of the extrapolation *versus* P and IT (MHz)	730.030 07	730.030 88
uncertainty (kHz)	3.24	3.20
slope of the straight line CLP *versus* P (MHz/W)	9×10^{-5}	-8×10^{-5}
final position of the line (MHz)	730.030 5(33)	
(interpolated position for a slope null)		
interpolated value for P/IT (arb. units)	0.236	
interpolated value for R_1	1.9 mm	

the variations of CLP with P. In practice, to obtain the position of the line, we use the following procedure: we make the mean of the linear extrapolations of CLP *versus* P and IT for two values of R_1 (for example 1.8 and 2 mm) and we interpolate these data to null the slope of the straight line $CLP(P)$. The details of this method are illustrated in Table 9 in the case of the $2S_{1/2}$–$8D_{3/2}$ transition in hydrogen. For this extrapolation, we have used the absolute frequency measurement described in Section 4 and the corrected line position CLP is not related to the FPR cavity but is an absolute frequency.

The uncertainties given in this table are only statistical. For each recording, the adjustement procedure gives an uncertainty for CLP which is deduced from the disagreement between the experimental and the theoretical curves. The linear extrapolation is made with a weighted least squares method. We calculate an *a priori* uncertainty σ_1 given by the propagation of the uncertainties of each record through the least squares calculations. This uncertainty does not depend on the dispersion of the points (CLP, P) with respect to a straight line. Next we calculate an *a posteriori* uncertainty σ_2 which takes into account this dispersion and is given by:

$$\sigma_2 = \sigma_1 t_{1\sigma} \sqrt{\frac{\chi^2}{n-2}}$$

where n is the number of recordings involved in the extrapolation and χ^2 the weighted least squares sum. The coefficient $t_{1\sigma}$ is estimated from the Student's t-distribution to obtain one standard deviation (*i.e.* $A\,(t_{1\sigma}|\,n-2) = 0.683$). Finally, we choose whichever value σ_1 and σ_2 which is largest.

We can test the consistency of our analysis by comparing, for several transitions, the interpolated values of P/IT and R_1 which correspond to the elimination of the variation of CLP with P. For example, the data obtained during the measurements of the 2S–8S/D transitions [6] are given in Table 10. The dispersion of the values of P/IT, which is not negligible, is probably due to the variation of the optical alignment of the experiment. We have also estimated directly this ratio from the light power transmitted by the enhancement cavity and the transmission of the end mirror of this cavity. We obtain the value $P = 0.259 \times IT$ with a typical uncertainty of 5%. This result is in acceptable agreement with the values given in Table 10. The same table also shows that the spatial distribution of the trajectories is more concentrated for deuterium (R_1 is smaller than for hydrogen). This is probably due to the larger quenching probability of the metastable deuterium atoms which are slower: the equipotential region where the metastable atoms are produced is reduced.

Table 10. Values of the slope of the straight line P *versus* IT and of the radius R_1 of the first diaphragm which correspond to the best determination of the light shift.

transition	R_1 (mm)	P/IT (arb. units)
hydrogen		
$2S_{1/2}$–$8D_{5/2}$	1.80	0.230
$2S_{1/2}$–$8D_{3/2}$	1.91	0.236
$2S_{1/2}$–$8S_{1/2}$	1.89	0.259
$2S_{1/2}$–$8D_{5/2}$	2.00	0.262
deuterium		
$2S_{1/2}$–$8D_{5/2}$	1.73	0.225
$2S_{1/2}$–$8D_{3/2}$	1.75	0.225
$2S_{1/2}$–$8S_{1/2}$	1.82	0.257

Some examples of the line width variations with the light power are shown in Figures 11a–11c in the case of the $2S_{1/2}$–$8S_{1/2}$, $2S_{1/2}$–$8D_{5/2}$ and $2S_{1/2}$–$12D_{5/2}$ transitions. The widths (full width at half maximum in terms of atomic frequency) deduced from the theoretical curves $L(\omega, P)$ correspond to the solid curves. We observe that the experimental widths are larger than the theoretical

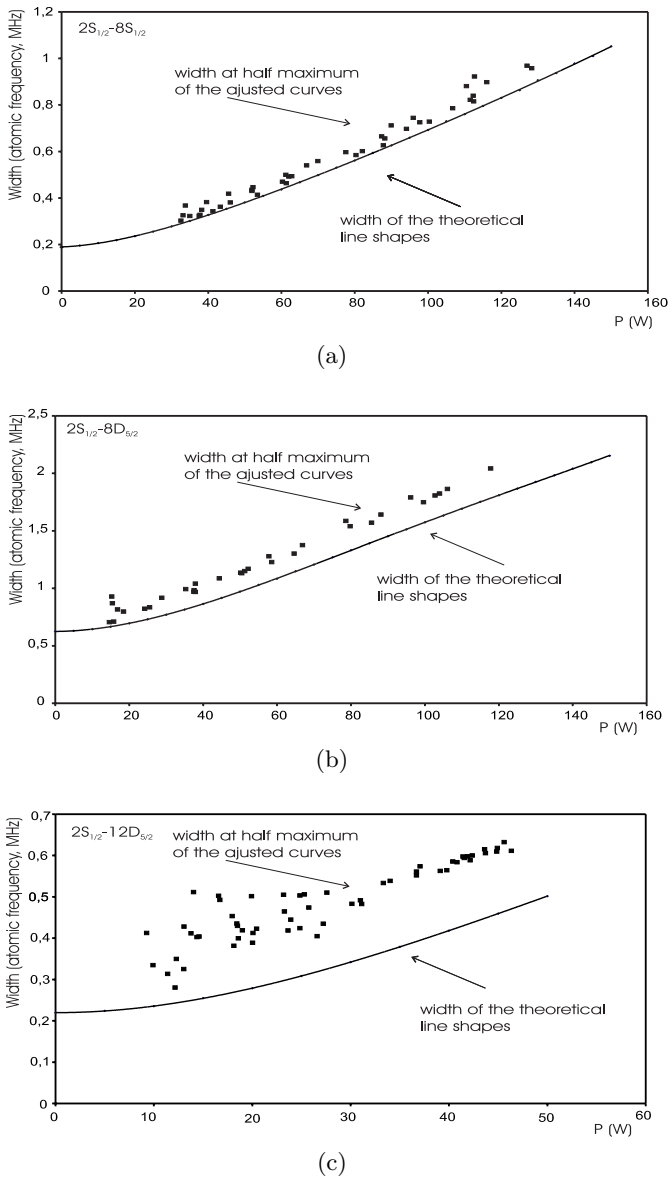

Fig. 11. Variation of the line width (full width at the half maximum in terms of atomic frequency) *versus* the light power P. (a) $2S_{1/2}(F = 1)$–$8S_{1/2}(F = 1)$ transition of hydrogen. (b) $2S_{1/2}(F = 1)$–$8D_{5/2}$ transition of hydrogen. (c) $2S_{1/2}(F = 1)$–$12D_{5/2}$ transition of hydrogen.

ones, especially for the 2S–nD transitions. These differences can be explained by the various effects which are not taken into account in the theoretical line shapes: the frequency jitter of the laser, the finite transit time, the residual Zeeman effect (for the 2S–nD transitions), black body radiation, the fluctuations of the light intensity seen by the atoms or the Stark effect due to stray electric fields.

Finally, to take into account the imperfections of our theoretical analysis, we introduce another uncertainty divided in two parts. (i) An uncertainty related to the optical alignment of the experiment. We have made a simulation of a bad alignment between the atomic beam and the laser beam [25] and we estimate this uncertainty to 4 kHz (in terms of atomic frequency). We consider that these uncertainties are correlated for a given series of extrapolations (for example the transitions 2S–8S/D in hydrogen, which are made in a relatively short time), but uncorrelated for the hydrogen and deuterium measurements and for the transitions with different principal quantum numbers. (ii) A theoretical uncertainty, common to all the measurements, which takes into account the possible incompleteness of our theoretical calculation. We have estimated this uncertainty from our results with different theoretical line shapes. For example, when we modified the theoretical calculations to include the ionisation of the upper level, the deviation of the atomic trajectories, or to reduce the step of the set of theoretical curves $L(\omega, P)$ from 10 W to 5 W, the shifts of the $2S_{1/2}$–$8D_{5/2}$ extrapolation in hydrogen were successively −640 Hz, 280 Hz and 1.4 kHz (in terms of atomic frequency). Finally, we have assumed that the effects neglected have the same order of magnitude and adopted a value of 2 kHz for this theoretical uncertainty.

3.3 Stark effect

3.3.1 Theoretical background

In our experiment, the stray electric fields are reduced to a few mV/cm thanks to the Aquadag coating. Nevertheless, as the matrix element of the Stark Hamiltonian $V_S = -\mathbf{d} \cdot \mathbf{E}$ ($\mathbf{E}$ is the electric field) varies with the principal quantum number as n^2, this small electric field can shift and broaden the lines, mainly for the 2S–12D transitions. The Stark coupling between the states $|nLJFm_F\rangle$ and $|nL'J'F'm'_F\rangle$ induces a quadratic Stark effect if $J \neq J'$ and a linear Stark effect if $J = J'$ which vary as n^7 and n^2 respectively. For instance, if we consider the energy levels for $n = 8$ (see Figs. 12a–12b), the quadratic Stark shift of the $8D_{5/2}$ level is due to the interaction with the $8P_{3/2}$ and $8F_{7/2}$ levels when the linear Stark effect is due to the mixing between the $8D_{5/2}$ and $8F_{5/2}$ levels. A straightforward second order calculation gives the quadratic Stark shift. As the anisotropic part of the quadratic Stark shift is small (7.6% and 1.8% for the $8D_{5/2}$ and $12D_{5/2}$ levels), we have considered only the scalar part of this shift (*i.e.* the mean shift for the m_F sublevels) which does not depend on the quantum number F. Table 11 gives the results for $n = 8$ and $n = 12$.

The linear Stark shift is more difficult to analyse. For example, the $8D_{5/2}$ and $8F_{5/2}$ hyperfine levels are mixed (see Fig. 12b) and these structures are smaller than the natural widths of the 8D and 8F levels (572 kHz and 285 kHz respectively). Consequently, in the experiment, we are not able to resolve these structures and we observe together the $8D_{5/2}$ and $8F_{5/2}$ levels. Nevertheless, to a first approximation, the shift of the line is null. If we assume that the effect of the electric field on the initial state g of the transition is negligible, the position ω_{tr}

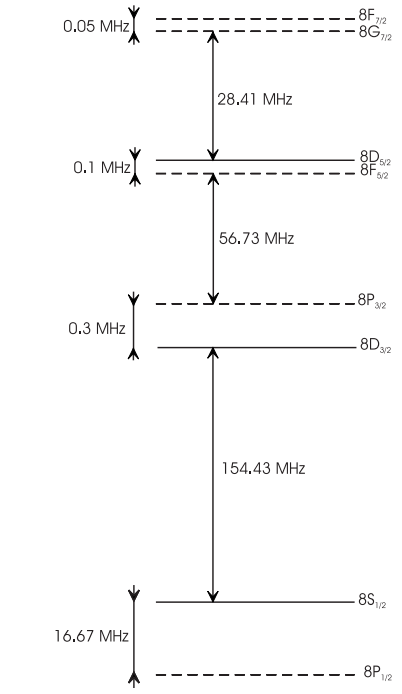

(a)

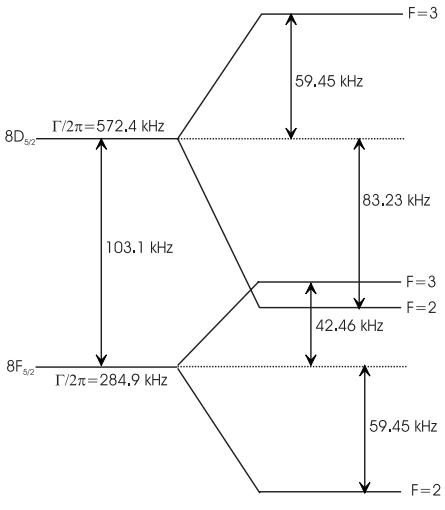

(b)

Fig. 12. (a) Fine structure and Lamb shifts of the 8S, 8P, 8D and 8F levels. The solid line corresponds to the levels which are excited with a two-photon transition from the metastable state. (b) Hyperfine structure of the $8D_{5/2}$ and $8F_{5/2}$ levels in hydrogen.

of the transition is:

$$\omega_{\rm tr} = \frac{\sum_i |\langle g| Q_{\rm tp} |\Psi_i\rangle|^2 \omega_i}{\sum_i |\langle g| Q_{\rm tp} |\Psi_i\rangle|^2} \tag{19}$$

where $Q_{\rm tp}$ is the two-photon operator (Eq. (8)), Ψ_i the eigenvectors with the energies $\hbar\omega_i$ of the Hamiltonian $H_0 + V_{\rm S}$ (H_0 being the Hamiltonian without electric field, $\hbar\omega_g$ the zero energy). Then we can write:

$$\omega_{tr} = \frac{\langle g| Q_{\rm tp}(H_0 + V_{\rm S}) P_e Q_{\rm tp}^+ |g\rangle}{\hbar \langle g| Q_{\rm tp} P_e Q_{\rm tp}^+ |g\rangle} \,. \tag{20}$$

We have introduced the projector on the subspace of the excited states $P_e = \sum_i |\Psi_i\rangle \langle\Psi_i|$. Then, because of parity conservation ($Q_{\rm tp}$ and $V_{\rm S}$ are respectively even and odd), we have $\langle g| Q_{\rm tp} V_{\rm S} P_e Q_{\rm tp}^+ |g\rangle = 0$ and the barycentre of the line does not depend on the electric field.

In our case, which is far more complicated, there are several limitations to the validity of this argument.

(i) Equation (19) does not take into account the strong saturation of the two-photon transition which modifies the weights of each component i.
(ii) We ignore the different natural widths of the upper states.
(iii) The adjustement procedure gives a line position which is not necessarily the barycentre of the line. For these reasons, we present now a line shape calculation taking into account the linear Stark effect.

Table 11. Coefficients of the quadratic Stark shift for some $n = 8$ and $n = 12$ levels.

level	quadratic Stark shift (MHz $V^{-2}cm^2$)
$8S_{1/2}$	77.69
$8P_{3/2}$	−39.11
$8D_{3/2}$	−36.29
$8D_{5/2}$	−53.59
$8F_{5/2}$	−45.28
$12P_{3/2}$	−698.10
$12D_{3/2}$	−684.87
$12D_{5/2}$	−1029.44
$12F_{5/2}$	−965.73

3.3.2 Line shape in presence of an electric field

The aim of this calculation is to consider simultaneously the natural width and the Stark coupling. The initial state g is coupled to a set of p states e (for instance the 12 sublevels $8D_{5/2}(F, m_F)$) by the optical excitation. The states e are mixed with the p states f (for instance the 12 sublevels $8F_{5/2}(F, m_F)$) by the Stark Hamiltonian $V_{\rm S}$. The evolution of the density operator ρ is:

$$\frac{{\rm d}\rho}{{\rm d}t} = \frac{1}{{\rm i}\hbar} \left[(H_0 + V_{\rm L} + V_{\rm S}), \rho \right] + \Gamma\rho \tag{21}$$

where the operators $V_{\rm L}$ and Γ describe the two-photon excitation and the spontaneous emission. We make the rotating wave approximation and we introduce the two-photon Rabi frequencies Ω_e:

$$\langle e| V_{\rm L} |g\rangle = \frac{\Omega_e}{2} \exp(-2{\rm i}\omega t),$$
$$\Omega_e = \frac{8\pi a_0^2 |\langle e| Q_{\rm tp} |g\rangle| I}{mc^2\alpha} \,. \tag{22}$$

If we assume that $\Omega_e \ll \Gamma_e$, we can neglect the populations and coherences $\rho_{ee'}$, $\rho_{ff'}$ or ρ_{ef} of the upper levels. In the rotating frame, we replace the density operator by an operator σ with $\sigma_{gg} = \rho_{gg}$, $\sigma_{eg} = \rho_{eg}\exp(2\mathrm{i}\omega t)$ and $\sigma_{ge} = \rho_{ge}\exp(-2\mathrm{i}\omega t)$ and we introduce the frequency detunings $\Delta_e = 2\omega - \omega_e$ and $\Delta_f = 2\omega - \omega_f$. In this way, we obtain from equation (21) a set of equations:

$$\frac{\mathrm{d}\sigma_{gg}}{\mathrm{d}t} = -\frac{\mathrm{i}}{2}\sum_e \Omega_e\left(\sigma_{eg} - \sigma_{ge}\right), \tag{23}$$

$$\frac{\mathrm{d}\sigma_{eg}}{\mathrm{d}t} = \left(\mathrm{i}\Delta_e - \frac{\Gamma_e}{2}\right)\sigma_{eg} - \mathrm{i}\frac{\Omega_e}{2}\sigma_{gg} - \frac{\mathrm{i}}{\hbar}\sum_f V_{ef}\sigma_{fg} \qquad (p \text{ equations}), \tag{24}$$

$$\frac{\mathrm{d}\sigma_{fg}}{\mathrm{d}t} = \left(\mathrm{i}\Delta_f - \frac{\Gamma_f}{2}\right)\sigma_{fg} - \frac{\mathrm{i}}{\hbar}\sum_e V_{fe}\sigma_{eg} \quad (p \text{ equations}). \tag{25}$$

We have introduced the matrix elements $V_{fe} = \langle f|\, V_{\mathrm{S}}\,|e\rangle$. Then we assume that the optical coherences σ_{eg} and σ_{fg} follow adiabatically the population σ_{gg}, *i.e.* that:

$$\frac{\mathrm{d}\sigma_{eg}}{\mathrm{d}t} = 0 \qquad \text{and} \qquad \frac{\mathrm{d}\sigma_{fg}}{\mathrm{d}t} = 0.$$

With these hypotheses, the equations (24, 25) become:

$$\left(\mathrm{i}\Delta_e - \frac{\Gamma_e}{2}\right)\sigma_{eg} + \sum_{e',f}\frac{V_{ef}V_{fe'}}{\hbar^2\left(\mathrm{i}\Delta_f - \Gamma_f/2\right)}\sigma_{e'g} = \mathrm{i}\frac{\Omega_e}{2}\sigma_{gg} \qquad (p \text{ equations}). \tag{26}$$

We obtain a set of p equations with p unknowns σ_{eg}. If we introduce the column vectors $[\sigma_{eg}]$ and $[\Omega_e/2]$, the set of equations (26) becomes:

$$A\left[\sigma_{eg}\right] = \mathrm{i}\left[\frac{\Omega_e}{2}\right]\sigma_{gg}$$

where the matrix elements of the $p \times p$ operator A are the coefficients of the set of equations (26). With these notations, the equation (23) becomes:

$$\frac{\mathrm{d}\sigma_{gg}}{\mathrm{d}t} = 2\,\mathrm{Re}\left[\frac{\Omega_e}{2}\right]^T A^{-1}\left[\frac{\Omega_e}{2}\right]\sigma_{gg}. \tag{27}$$

This equation describes the evolution of the population σ_{gg} and, finally, the two-photon transition probability Γ_g is:

$$\Gamma_g = -2\,\mathrm{Re}\left[\frac{\Omega_e}{2}\right]^T A^{-1}\left[\frac{\Omega_e}{2}\right]. \tag{28}$$

This equation is the equivalent, in the case of the Stark mixing, of equation (9). The two-photon probability is proportional to I^2 and we can separate the frequency and intensity variations:

$$\Gamma_g = I^2\gamma_g(\omega)$$

where $\gamma_g(\omega)$ describes the line profile. Afterwards we include the light shifts, but we neglect the photoionisation and the saturation of the two-photon transition probability. Strictly speaking, we should replace each atomic frequency ω_i ($i = g$, e or f) by $\omega_i - c_{\mathrm{ls}}(i)I$, where the light shift coefficient depends on the state i. In actual fact, to reduce the calculation time, we assume that all the states e and f have the same light shift coefficient c_{ls}. This is justified for two reasons: (i) the anisotropy of the light shift is small (see Tab. 4); (ii) the light shift coefficients of the levels nP, nD and nF are all very similar. For instance, the light shift coefficients β_e of the states 8P($m_L = 0$), 8D($m_L = 0$) and 8F($m_L = 0$) are respectively 287.78, 285.43 and 281.1 (in atomic units). With this approximation, when we include the light shift, the transition probability becomes:

$$\Gamma_g = I^2\gamma_g(\omega - \frac{1}{2}c_{\mathrm{ls}}I). \tag{29}$$

This equation replaces equation (10). Then we follow the procedure described in Section 3.1 (Eqs. (16–18)). However,we have not summed over the velocity distribution in equation (18) but used instead the mean velocity v_m [11]:

$$1/v_m = \langle 1/v\rangle = \frac{\displaystyle\int_0^\infty \frac{f(v)}{v}\mathrm{d}v}{\displaystyle\int_0^\infty f(v)\mathrm{d}v}$$

where $f(v)$ is the velocity distribution (Eq. (1)).

In reality, we do not know the orientation of the stray electric fields. Consequently, we have made the line shape calculation for an electric field either parallel or perpendicular to the laser polarisation to obtain the line shapes $L_\parallel(\omega, P, E)$ and $L_\perp(\omega, P, E)$ ($E = |\mathbf{E}|$). Moreover we have to consider the case of each hyperfine sublevel m_F of the $2\mathrm{S}_{1/2}(F = 1)$ level ($2\mathrm{S}_{1/2}(F = 3/2)$ for deuterium). Finally, we evaluate the mean of these different profiles:

$$L(\omega, P, E) = \frac{1}{2F+1}\sum_{m_F}\left[\frac{1}{3}L_{\parallel,m_F}(\omega, P, E) + \frac{2}{3}L_{\perp,m_F}(\omega, P, E)\right].$$

Figure 13 shows an example of this line shape in the case of the $2\mathrm{S}_{1/2}(F{=}3/2)$–$20\mathrm{D}_J$ transition in deuterium for a light power of 20 W and several electric fields (in this calculation we have neglected the quadratic Stark effect between the $J = 3/2$ and $J = 5/2$ levels). For an electric field of 5 mV/cm, the linear Stark structure appears clearly and we see that the $n\mathrm{D}_{3/2}$ level is more sensitive to an electric field than the $n\mathrm{D}_{5/2}$.

3.3.3 Corrections due to the Stark effect

As the linear Stark effect varies as n^2, we can estimate the residual electric fields from the widths of the transitions to higher nD levels. During the measurements

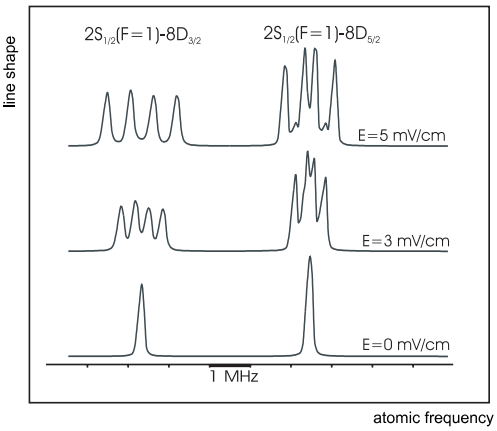

Fig. 13. Stark splitting of the $2S_{1/2}(F = 3/2)$–$20D_{3/2}$ and –$20D_{5/2}$ transitions for several electric fields.

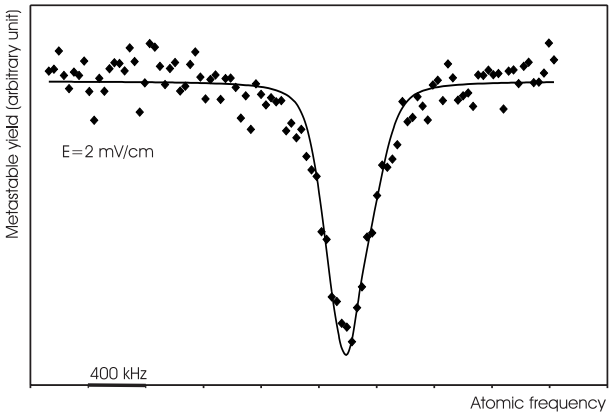

Fig. 14. Fit of the $2S_{1/2}(F = 3/2)$–$15D_{3/2}$ two-photon transition in deuterium. The theoretical curve (solid) is calculated with an electric field of 2 mV/cm.

of the 2S–8S/D frequencies [5,6], we have made several recordings of the $2S_{1/2}$–$15D_J$ transition. For the 2S–12D measurements [8], we have also observed the $2S_{1/2}$–$20D_J$ lines. To determine the electric field, we adjust the profile $L(\omega, P, E)$ to the experimental data for several values of the electric field E. We use the procedure described in Section 3.2, but without the Gaussian broadening ($\Delta_\omega = 0$). Two examples are given in Figures 14 and 15. For the $2S_{1/2}$–$15D_{3/2}$ transition (Fig. 14), the best fit is obtained for an electric field of about 2 mV/cm. Figure 15 shows the fit of the $2S_{1/2}$–$20D_J$ with an electric field of 3 mV/cm. In this case we see the structure of the theoretical curve (in the experiment, we have in fact a distribution of the amplitude E), but the experimental lines are narrower than the theoretical ones. Finally, we can estimate the residual electric field E_R to be 2.5(1.0) mV/cm during the 2S–8S/D measurements [6] and 2.0(1.0) mV/cm for the 2S–12D ones [8].

The calculation of the quadratic Stark effect is straightforward (see Tab. 11). To evaluate the corrections due to the linear Stark effect, we have fitted all the experimental curves $2S_{1/2}$–$8D_J$ and $2S_{1/2}$–$12D_J$ with the theoretical profiles $L(\omega, P, E)$ for the electric field $E = 0$ and $E = E_R$ (for the calculation of $L(\omega, P, E)$ we have used $R_1 = 2$ mm). Then, we make the difference between the two extrapolated values of CLP (obtained for $E = 0$ and $E = E_R$) to obtain the shift due to the linear Stark effect. These corrections are given in Table 12. We can make two comments.

(i) Contrary to the result of equation (20), the shift due to the linear Stark effect is not zero: the $nD_{5/2}$ level is shifted up, and the $nD_{3/2}$ shifted down. We have the following explanation. Schematically, as the $nD_{5/2}$ level is above the $nF_{5/2}$, the mixing of the two levels divides the two-photon line in two components, a large component above the $nD_{5/2}$ level and a small component below the $nF_{5/2}$ level. Following equation (20), the barycentre of these two components is not shifted. If we take into account the saturation of the two-photon transition, the large component is reduced more than the small component and the barycentre should be down shifted. In fact we observe a shift of opposite sign: the adjustment procedure does not give the barycentre of the line, but rather makes the fit to the main component, which is up shifted. The explanation is similar for the $nD_{3/2}$ level but with the signs reversed.

(ii) The total shift is larger for the $nD_{3/2}$ level than for the $nD_{5/2}$, because the quadratic and the linear Stark shift have the same signs in the former case and opposite signs in the latter. This result is important for the 2S–12D transitions: the correction and the uncertainty due to the Stark effect are significant for the $2S_{1/2}$–$12D_{3/2}$ transition and smaller for the $2S_{1/2}$–$12D_{5/2}$ one (see Tab. 12).

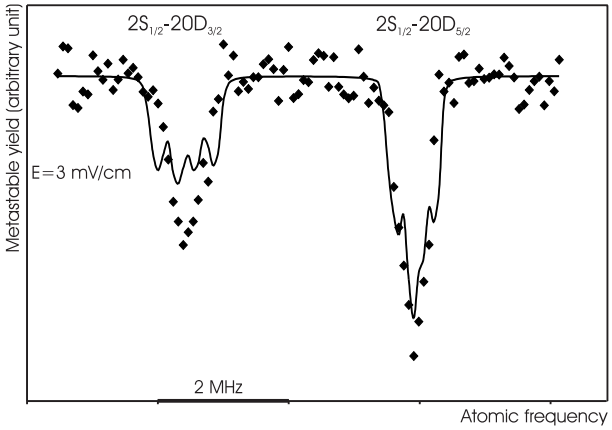

Fig. 15. Fit of the experimental $2S_{1/2}(F = 3/2)$–$20D_{3/2}$ and –$20D_{5/2}$ profiles in deuterium. The theoretical curve (solid) is calculated with an electric field of 3 mV/cm. For the $2S_{1/2}(F = 3/2)$–$20D_{3/2}$ transition, the experimental curve is narrower than the theoretical one.

Table 12. Corrections due to the Stark effect for the 2S–8S/D and 2S–12D transitions (the quadratic Stark corrections are similar for hydrogen and deuterium).

transition	E_R (mV/cm)	quadratic Stark effect (kHz)	linear Stark effect (kHz)	total shift (kHz)
$2S_{1/2}$–$8S_{1/2}$	2.5(1.0)	0.56(40)		0.56(40)
hydrogen				
$2S_{1/2}$–$8D_{3/2}$	2.5(1.0)	−0.27(19)	−0.24(14)	−0.51(33)
$2S_{1/2}$–$8D_{5/2}$	2.5(1.0)	−0.36(25)	0.54(38)	0.18(13)
deuterium				
$2S_{1/2}$–$8D_{3/2}$	2.5(1.0)	−0.27(19)	−0.59(43)	−0.86(62)
$2S_{1/2}$–$8D_{5/2}$	2.5(1.0)	−0.36(25)	0.38(26)	0.02(1)
hydrogen				
$2S_{1/2}$–$12D_{3/2}$	2.0(1.0)	−3.4(2.8)	−2.6(2.1)	−6.0(4.9)
$2S_{1/2}$–$12D_{5/2}$	2.0(1.0)	−5.0(4.0)	2.9(2.8)	−2.1(1.2)
deuterium				
$2S_{1/2}$–$12D_{3/2}$	2.0(1.0)	−3.4(2.8)	−2.7(2.6)	−6.1(5.4)
$2S_{1/2}$–$12D_{5/2}$	2.0(1.0)	−5.0(4.5)	3.9(3.6)	1.1(1.0)

4 Optical frequency measurements

4.1 The rubidium frequency standard

4.1.1 Experimental arrangement and metrological properties

The cornerstone of our optical frequency measurements is a new standard, namely a laser diode at 778 nm (*i.e.* a frequency ν of 385 THz) stabilized to the $5S_{1/2}$–$5D_{5/2}$ two-photon transition of rubidium (LD/Rb laser). This standard has been described previously elsewhere [7,26,27]. The AlGaAs laser diode is used in an extended cavity configuration to obtain a typical spectral width of 100 kHz. The rubidium cell (temperature of 90 °C and pressure of about 8×10^{-5} torr) is placed in an enhancement cavity (30 cm long with a beam waist of 420 μm) in order to define well the two counterpropagating Gaussian beams and eliminate completely the first order Doppler effect. The optical isolation between the laser and the cavity is provided by a Faraday isolator (isolation of 60 dB) and an acousto-optic modulator (AOM) in a double-pass configuration. To control the light shift, we stabilize with the AOM the intensity of the beam transmitted by the cavity to a reference value I_R. The two-photon transition is monitored *via* the fluorescence at 420 nm due to the cascade 5D–6P–5S. The frequency lock of this system is made with two servo-loops. The laser frequency is modulated at 100 kHz with a peak-to-peak amplitude of 300 kHz. A first error signal is extracted from the intensity of the transmitted beam by the cavity to lock the cavity length to the laser wavelength. We then detect the modulation of the fluorescence signal to lock the laser frequency to the two-photon transition of rubidium.

Three identical systems have been built, two at the LPTF (labelled L_1 and L_2) and a third in *Laboratoire Kastler Brossel* (labelled KB). As the two laboratories are linked by two, 3 km long, optical fibers, we can compare the frequencies of the three systems. To check the frequency shift due to the fiber, we have used our highly stabilized titanium-sapphire laser. After a round trip of 6 km through the fibers, we have observed a maximum frequency shift of 3 Hz [28]. This shift is completely negligible for our frequency measurements. From these frequency comparisons, we have determined precisely the light shift of each system (−7.32 kHz for the KB system with the intensity reference value I_R). The main metrological features of the LD/Rb laser are a frequency stability (Allan variance) of about $4\times10^{-13}\tau^{-1/2}$ per laser over 1000 s and a day-to-day repeatability of 400 Hz.

4.1.2 Optical frequency measurement

The frequencies of the three LD/Rb lasers stabilized on the $5S_{1/2}(F{=}3)$–$5D_{5/2}(F{=}5)$ two-photon transition of ^{85}Rb were measured in 1996 at the LPTF with a frequency chain. This frequency chain connects the LD/Rb laser at 385 THz to a standard at 29 THz, namely a CO_2 laser stabilized to an osmium tetraoxyde line (CO_2/OsO_4) [7]. This standard had been previously measured in 1985 with respect to the Cs clock with an uncertainty of 70 Hz (ν = 29 096 274 952 340 (70) Hz) [29,30]. The optical frequencies of the three LD/Rb systems have been found to lie very close to each other (the maximum difference was 1.1 kHz) and the measured frequency of the system working at LKB was, after correction for the light shift:

$$\nu_{KB} = 385\ 285\ 142\ 377.82\ \text{kHz} \qquad (30)$$

with an uncertainty of 1 kHz. This uncertainty was due to the CO_2 laser (13×70 Hz) and the day-to-day repeatability of the LD/Rb standard (400 Hz).

To keep this precision, we have made several frequency comparisons between the L_1, L_2 and KB systems. In 1998, for instance, we have measured the frequency difference $\nu_{KB} - \nu_{L_1}$ and $\nu_{KB} - \nu_{L_2}$. If we suppose that there was no drift of the frequencies ν_{L_1} or ν_{L_2} between 1996 and

1998, we can deduce two values for the frequency of the KB system:

$$\nu_{\mathrm{KB}}(\mathrm{L}_1) = 385\ 285\ 142\ 377.53\ \mathrm{kHz},$$

$$\nu_{\mathrm{KB}}(\mathrm{L}_2) = 385\ 285\ 142\ 378.32\ \mathrm{kHz}.$$

These values are very close to that of the 1996 measurement (Eq. (30)) so we estimate the frequency shift of the KB system to be smaller than 500 Hz.

In 1998, the measurement of the CO_2/OsO_4 standard with respect to the Cs clock was remade with an uncertainty of 20 Hz (*i.e.* a relative uncertainty of 7×10^{-13}) [31]. This measurement corrects the previous one by −88 Hz. With this correction, the frequency of the LD/Rb standard of LKB becomes:

$$\nu_{\mathrm{KB}} = 385\ 285\ 142\ 376.68\ \mathrm{kHz}.$$

Finally, if we take into account the light shift, the frequency $\nu_{\mathrm{KB}}(I_{\mathrm{R}})$ of the LD/Rb standard of LKB working with the reference intensity I_{R} is:

$$\nu_{\mathrm{KB}}(I_{\mathrm{R}}) = 385\ 285\ 142\ 369.4\ (1.0)\ \mathrm{kHz}. \qquad (31)$$

It is this value which has been used for the analysis of the 2S–8S/D and 2S–12D measurements. We have kept a conservative uncertainty of 1 kHz which takes into account the day-to-day repeatability (400 Hz), the long term stability of the LD/Rb standard (500 Hz) and the accuracy of the CO_2/OsO_4 standard (13×20 Hz).

4.2 Optical frequency measurements of the 2S–8S and 2S–8D transitions

4.2.1 The first measurement of the 2S–8S and 2S–8D transitions

In 1993 we carried out a first optical frequency measurement of the 2S–8S and 2S–8D two-photon transitions [5,32]. The principle of this measurement was the near coincidence between the 2S–8S/D frequencies and the frequency difference of two standard lasers, the iodine stabilized (He–Ne/I_2) and the methane stabilized (He–Ne/CH_4) helium-neon lasers (frequencies ν_f and $\nu_{\mathrm{CH_4}}$ respectively):

$$\nu(2\mathrm{S}{-}8\mathrm{S/D}) = \nu_f - \nu_{\mathrm{CH_4}} + \Delta_1$$

where the residual frequency difference Δ_1 is about 89 GHz. After a short description of our experimental scheme, we present an up-to-date analysis of the data which takes into account the recent improvements of the line shape calculations and some optical frequency measurements made subsequently with the LD/Rb standard.

Figure 16 shows the experimental set-up. We use two titanium-sapphire lasers labelled TiS1 and TiS2 which are frequency shifted by about Δ_1. We observe the two-photon transition in hydrogen with the first titanium-sapphire laser. As the power of the He–Ne/CH_4 laser is only 100 μW, we use a more powerful (about 15 mW) auxiliary He–Ne laser at 3.39 μm, which is frequency locked to the He–Ne/CH_4 standard laser. Then the second titanium-sapphire laser and the auxiliary He–Ne laser are mixed in a $LiIO_3$ crystal to generate a radiation at 633 nm. This light is heterodyned with that of the He–Ne/I_2 standard laser. Finally, the frequency difference Δ_1 between the two titanium-sapphire lasers is measured with a Schottky diode which is simultaneously illuminated by the two titanium-sapphire lasers and a Gunn diode at 89 GHz. From the frequency Δ_1 and that of the beat notes at 3.39 μm and 633 nm, we deduce the optical frequency of the TiS1 laser. The details of these frequency measurements are given in references [5,15].

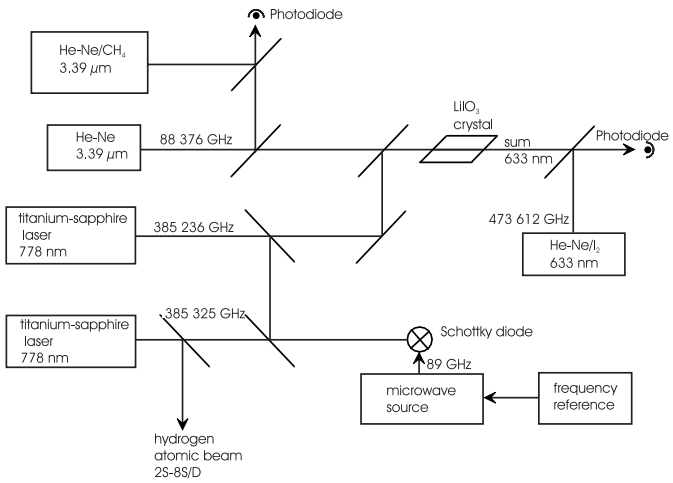

Fig. 16. Experimental set-up for the frequency comparison between the 2S–8S/D transitions in hydrogen and the methane stabilized and iodine stabilized standard lasers.

The He–Ne/CH_4 standard laser was the laser VB-BIPM from the *Bureau International des Poids et Mesures*. Its frequency is known from previous measurements with an uncertainty of 1 kHz:

$$\nu_{\mathrm{CH_4}} = 88\,376\,181\,602.6\,(1.0)\ \mathrm{kHz}.$$

The He–Ne/I_2 standard laser was the laser INM12 from the *Institut National de Métrologie*. In 1992, the frequency ν_f of INM12 laser (locked on the f hyperfine component of the $^{127}I_2$ R11-5 iodine line) was measured in the LPTF with respect to the CO_2/OsO_4 standard [33]. The measured frequency was:

$$\nu_f = 473\ 612\ 353\ 586.9(3.4)\ \mathrm{kHz}. \qquad (32)$$

In 1993 we used these frequency values to determine the hydrogen frequencies. Today, we can use a more reliable value of the frequency ν_f of the INM12 laser. First, in 1993, promptly after the hydrogen measurements, we measured the frequency $\nu_{\mathrm{Rb}}(5\mathrm{S}_{1/2}{-}5\mathrm{D}_{3/2})$ of the $5\mathrm{S}_{1/2}{-}5\mathrm{D}_{3/2}$ two-photon transition of rubidium with the same frequency chain [34]. Indeed, we have a similar coincidence:

$$\nu_{\mathrm{Rb}}(5\mathrm{S}_{1/2}{-}5\mathrm{D}_{3/2}) = \nu_f - \nu_{\mathrm{CH_4}} + \Delta_2 \qquad (33)$$

Table 13. Experimental determination of the 2S–8S/D transition frequencies from our 1993 measurements (all values in MHz).

transition	$2S_{1/2}$–$8S_{1/2}$	$2S_{1/2}$–$8D_{3/2}$	$2S_{1/2}$–$8D_{5/2}$
1993 analysis [5]	770 649 306.3195	770 649 460.0438	770 649 517.1844
updated analysis	770 649 306.3187	770 649 460.0467	770 649 517.1887
correction of ν_f	0.0070	0.0070	0.0070
$2S_{1/2}$ hyperfine shift	44.3892	44.3892	44.3892
$8S_{1/2}$ hyperfine shift	−0.6936		
$\nu(2S_{1/2}$–$8S_{1/2}/8D_J)$	770 649 350.0213	770 649 504.4429	770 649 561.5849
$8S_{1/2}/8D_{3/2}$–$8D_{5/2}$ splitting	211.5621	57.1291	
$\nu(2S_{1/2}$–$8D_{5/2}) - 770\,649\,000$	561.5834 (143)	561.572 (131)	561.5849 (123)
mean value		770 649 561.580 (11)	

but in this case the residual frequency Δ_2 is only 4 to 7 GHz. For instance, for the $5S_{1/2}(F = 1)$–$5D_{3/2}(F = 3)$ hyperfine component in ^{87}Rb, we have measured $\Delta_2 = 7\,383\,160.2\,(2.0)$ kHz. Afterwards, the fine structure $5D_{3/2}$–$5D_{5/2}$ in rubidium was measured at the LPTF [35]. The frequency difference between the ^{85}Rb $5S_{1/2}(F = 3)$–$5D_{5/2}(F = 5)$ (*i.e.* the frequency of the LD/Rb standard) and ^{87}Rb $5S_{1/2}(F = 1)$–$5D_{3/2}(F = 3)$ hyperfine components was measured to be 41 587 229.1 (2.0) kHz. Finally, if we take into account the frequency measurement of the LD/Rb standard, we can deduce the frequency $\nu_{\rm Rb}(5S_{1/2}$–$5D_{3/2})$ and use equation (33) to obtain the frequency ν_f of the He–Ne/I_2 INM12 standard. The result is:

$$\nu_f = 473\ 612\ 353\ 590.4(3.5)\ \text{kHz}. \qquad (34)$$

We have used the mean value of the three LD/Rb standard lasers L_1, L_2 and KB corrected for the recent measurement of the CO_2/OsO_4 standard [7,31] (*i.e.* $\nu(\text{LD/Rb}) = 385\,285\,142\,377.1\,(2.0)$ kHz). The obtained ν_f value is up shifted (3.5 kHz) with respect to the 1992 measurement (Eq. (32)). Though the uncertainties are similar, the value given by equation (34) seems the most reliable because of the very good reproducibility of the two-photon rubidium lines.

In 1993, we measured the three $2S_{1/2}$–$8S_{1/2}$, $2S_{1/2}$–$8D_{3/2}$ and $2S_{1/2}$–$8D_{5/2}$ two-photon transitions in hydrogen (see Tab. 2). We have remade the analysis of the data with the line shape calculations presented in Section 3. The hyperfine structure of the 8D levels, the photoionisation of the excited level, the saturation of the two-photon transition as well as the second order Doppler effect are included in the theoretical profile. The details of this analysis are given in Table 13. We recall the results of our first analysis made in 1993 (first row of the table). The results, given in terms of atomic frequency, are corrected for the second order Doppler effect and the hyperfine structure of the D levels (we have detected an error in the reference [5]: the correction due to the second order Doppler effect is not 40.2 kHz, but rather 42.4 kHz, as indicated in Tab. 1). These values can be directly compared with those of our up-to-date analysis (second row of the table). The result is similar for the $2S_{1/2}$–$8S_{1/2}$ transition, but is upshifted by about 3 kHz for the $2S_{1/2}$–$8D_J$ ones. After the correction of the He–Ne/I_2 frequency (see Eqs. (32, 34)) and of the hyperfine structure of the S levels, we obtain the $2S_{1/2}$–$8S_{1/2}$ and $2S_{1/2}$–$8D_J$ splittings (for this analysis we neglect the Stark effect and the shift due to the black body radiation). For the $2S_{1/2}$ hyperfine structure, we use the value of reference [36]. We deduce the $8S_{1/2}$ hyperfine structure with a simple $1/n^3$ scaling law, because at this level of precision the relativistic corrections in $(Z\alpha)^2$ are negligible. The three experimental values of the $2S_{1/2}$–$8S_{1/2}$ and $2S_{1/2}$–$8D_J$ splittings can be intercompared using the theoretical values of the fine structure and of the Lamb shifts in the $n = 8$ levels. Table 14 gives the theoretical Lamb shifts useful in this paper. We have taken into account the more precise values of the Bethe logarithms [37] and all the recent calculations of the high-order terms following the references [38–40]. For the nuclear charge radii in hydrogen and deuterium, we have used $r_{\rm p} = 0.862$ fm and $r_{\rm d} = 2.115$ fm [41,42]. This enables us to deduce three independent values for the $2S_{1/2}$–$8D_{5/2}$ splitting which are in good mutual agreement (see Tab. 13). The quoted uncertainties come from the statistics, the second-order Doppler effect (2 kHz), the optical alignment and the theoretical line shape (4 kHz and 2 kHz respectively, see Sect. 3.2) and the He–Ne/I_2 standard laser (2×3.5 kHz, see Eq. (34)). Finally, the mean value is:

$$\nu(2S_{1/2}-8D_{5/2}) = 770\,649\,561.580\,(11)\ \text{MHz}.$$

Table 14. Theoretical Lamb shifts in hydrogen and deuterium.

level	hydrogen (MHz)	deuterium (MHz)
$3S_{1/2}$	311.4040 (20)	311.8106 (20)
$6S_{1/2}$	39.0860 (3)	39.1368 (3)
$6D_{5/2}$	0.1660 (2)	0.1662 (2)
$8S_{1/2}$	16.5008 (3)	16.5222 (3)
$8D_{3/2}$	−0.0607 (2)	−0.0607 (2)
$8D_{5/2}$	0.0714 (2)	0.0715 (2)
$12D_{3/2}$	−0.0176 (2)	−0.0176 (2)
$12D_{5/2}$	0.0215 (2)	0.0215 (2)

Table 15. Experimental determination of the 2S–8S/D transition frequencies from the measurements made in hydrogen with the rubidium standard. All the values are in MHz and we have subtracted a frequency ν_0 of 770 649 GHz. The values in bold-faced type are the ones used in the 1998 CODATA adjustment of the fundamental constants [44].

transition in hydrogen	$2S_{1/2}$–$8S_{1/2}$	$2S_{1/2}$–$8D_{3/2}$	$2S_{1/2}$–$8D_{5/2}$
result of the extrapolation $-\nu_0$	306.3175 (70)	460.0609 (66)	517.1958 (40)
stark effect	−0.0006 (4)	0.0005 (3)	−0.0002 (1)
black body radiation	−0.0005 (1)	−0.0006 (2)	−0.0006 (2)
$2S_{1/2}$ hyperfine shift	44.3892	44.3892	44.3892
$8S_{1/2}$ hyperfine shift	−0.6936		
$\nu(2S_{1/2}$–$8S_{1/2}/8D_J)-\nu_0$	**350.0120 (86)**	**504.4500 (83)**	**561.5842 (64)**
$8S_{1/2}/8D_{3/2}$–$8D_{5/2}$ splitting	211.5621	57.1291	
$\nu(2S_{1/2}$–$8D_{5/2})-\nu_0$	561.5741 (86)	561.5791 (83)	561.5842 (64)
mean value and χ^2	770 649 561.5811 (59)		$\chi^2 = 1.69$

By comparison with the published value in 1993 ($\nu(2S_{1/2}$–$8D_{5/2}) = 770\,649\,561.567$ (10) MHz [5]), there is a difference of 13 kHz due to the error in the calculation of the second-order Doppler effect (2.2 kHz), the frequency of the He–Ne/I_2 standard laser (7 kHz), the improvements of the theoretical line shape (2.6 kHz) and the more precise Bethe logarithms (1.2 kHz).

4.2.2 The 1996 measurement using the rubidium standard

To take advantage of the very good long term stability of the LD/Rb standard laser, we have remade the optical frequency measurements of the 2S–8S and 2S–8D transitions in hydrogen and deuterium [6,25]. In this case, the link between the hydrogen frequencies and the standard laser is straightforward. We have:

$$\nu(2S{-}8S/D) = \nu(LD/Rb) + \Delta_3$$

where the residual difference Δ_3 is about 40 GHz in hydrogen and 144 GHz in deuterium. To measure this frequency difference, we focus on a Schottky diode the titanium-sapphire laser (used for the observation of the hydrogen lines) and the LD/Rb standard laser. The Schottky diode is simultaneously irradiated by a microwave source at 13 GHz for hydrogen and 48.4 GHz for deuterium. We detect the low frequency beat note between the two optical radiations and the third harmonic of the microwave. Typically, the signal-to-noise ratio is 35 dB with a resolution bandwidth of 300 kHz. A tracking oscillator is phase locked to this beat note, and we count continuously this frequency. The 13 GHz source is the 130th harmonic of a very stable quartz oscillator at 100 MHz (we use a step recovery diode, a YIG filter and a 35 dB amplifier). For deuterium, this microwave source is shifted to 12.1 GHz (on the 121th harmonic of the 100 MHz quartz). Then, a Gunn diode at 48.4 GHz is phase locked on the fourth harmonic of the 12.1 GHz source. The frequency of the 100 MHz quartz oscillator is continuously compared to a high stability quartz oscillator at 10 MHz (stability of 4×10^{-9} during four months), which has been measured with a hydrogen maser several times. Finally, the uncertainty on the Schottky diode measurement is about 15 Hz in hydrogen and 50 Hz in deuterium.

We have measured the three $2S_{1/2}$–$8S_{1/2}$, $2S_{1/2}$–$8D_{3/2}$ and $2S_{1/2}$–$8D_{5/2}$ two-photon transitions in hydrogen and deuterium (see Tab. 2). In hydrogen, the $2S_{1/2}$–$8D_{5/2}$ frequency was measured twice, at the beginning and at the end of the experiment. The analysis of the results is made in Tables 15 and 16. We use the same procedure than for the 1993 results, but we include the corrections due to the Stark effect and the black body radiation (see Tabs. 12 and 8). In deuterium, we have used the $2S_{1/2}$ hyperfine structure given in reference [43]. In addition to the uncertainties quoted in the Tables, the final uncertainties take into account the second-order Doppler effect (1 kHz), the measurement and the long term stability of the LD/Rb standard laser (2 kHz), the optical alignment and the theoretical line shape (4 kHz and 2 kHz respectively, see Sect. 3.2). The three transition frequencies in hydrogen and deuterium, in bold-faced type in the tables, were used in the 1998 CODATA adjustment of the fundamental constants [44]. As in Table 13, we use the theoretical values of the fine structure between the $8D_{5/2}$ level and the $8S_{1/2}$ or $8D_{3/2}$ ones to obtain three independent values of the $2S_{1/2}$–$8D_{5/2}$ interval. These values are in good agreement with each other, especially these for deuterium. The comparison with the results of 1993 in hydrogen (see Tab. 13) shows an improvement of the accuracy by about a factor 2 and a perfect agreement between the mean values of the $2S_{1/2}$–$8D_{5/2}$ frequencies. The results given in the Tables 15 and 16 are slightly different from the ones published previously [6] (for the mean values, −3.9 kHz and −3.2 kHz in hydrogen and deuterium). These differences are due to the new measurement of the CO_2/OsO_4 laser (−2.3 kHz), the corrections due to the Stark effect and the black body radiation (about −0.6 kHz) and some improvements of the theoretical line shape. With respect to reference [6], the uncertainties are also more conservative.

4.3 Optical frequencies measurements of the 2S–12D transitions

In order to test the measurements of the 2S–8S and 2S–8D transitions, we have built a new frequency chain to measure the frequencies of the 2S–12D intervals [8,45].

Table 16. Experimental determination of the 2S–8S/D transition frequencies from the measurements made in deuterium with the rubidium standard. All the values are in MHz and we have subtracted a frequency ν_0 of 770 859 GHz. The values in bold-faced type are the ones used in the 1998 CODATA adjustment of the fundamental constants [44].

transition in deuterium	$2S_{1/2}$–$8S_{1/2}$	$2S_{1/2}$–$8D_{3/2}$	$2S_{1/2}$–$8D_{5/2}$
result of the extrapolation $-\nu_0$	27.8184 (47)	182.0600 (38)	239.2086 (32)
stark effect	−0.0006 (4)	0.0009 (6)	$\simeq 0$
black body radiation	−0.0005 (1)	−0.0006 (2)	−0.0006 (2)
$2S_{1/2}$ hyperfine shift	13.6415	13.6415	13.6415
$8S_{1/2}$ hyperfine shift	−0.2131		
$\nu(2S_{1/2}$–$8S_{1/2}/8D_J)-\nu_0$	**41.2457 (69)**	**195.7018 (63)**	**252.8495 (59)**
$8S_{1/2}/8D_{3/2}$–$8D_{5/2}$ splitting	211.6027	57.1448	
$\nu(2S_{1/2}$–$8D_{5/2})-\nu_0$	252.8484 (69)	252.8466 (63)	252.8495 (59)
mean value and χ^2	770 859 252.8483 (55)		$\chi^2 = 0.34$

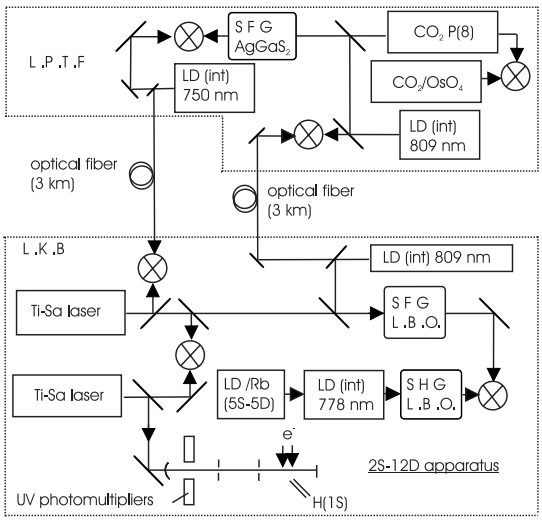

Fig. 17. Outline of the frequency chain between the 2S–12D hydrogen frequencies and the LD/Rb and CO_2/OsO_4 standards. The details are explained in the text (Ti-Sa: titanium sapphire laser, LD/Rb: rubidium stabilized laser diode, LD(int): intermediate laser diode, CO_2/OsO_4: osmium tetraoxyde stabilized CO_2 laser, SHG: second harmonic generation, SFG: sum frequency generation).

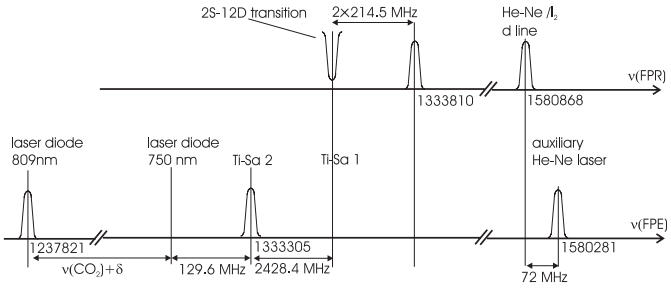

Fig. 18. Example of the position of the laser frequencies with respect to the FPR and FPE cavities during the measurements of the 2S–12D transitions. The fringe 1 580 868 of the FPR cavity is locked on the d line of the He–Ne/I_2 standard laser. The first titanium sapphire laser (Ti-Sa1) is locked on the fringe 1 333 810 of the FPR cavity with an offset of 2×214.5 MHz. The 809 nm laser diode, the second titanium sapphire laser (Ti-Sa2) and the auxiliary He–Ne laser are respectively locked on the fringes 1 237 821, 1 333 305 and 1 580 281. The laser diode at 750 nm is frequency shifted by $\nu(CO_2)+\delta$ with respect to the one at 809 nm.

This transition yields complementary information, because the 12D levels are very sensitive to the stray electric fields (the quadratic Stark shift varies as n^7, see Sect. 3.3), and so such a measurement provides a stringent test of Stark corrections to the Rydberg levels.

4.3.1 The experimental scheme

The frequency difference between the 2S–12D transitions ($\lambda \approx 750$ nm, $\nu \approx 399.5$ THz) and the LD/Rb standard laser is about 14.2 THz, *i.e.* the half of the frequency of the CO_2/OsO_4 standard. To bisect this frequency we use an optical divider [2,46]. The frequency chain (see Fig. 17) is split between the LPTF and the LKB: the two optical fibers are used to transfer the CO_2/OsO_4 standard from the LPTF to the LKB, where we observe the hydrogen transitions. This chain includes an auxiliary source at 809 nm ($\nu \approx 370.5$ THz) such that the laser frequencies satisfy the equations:

$$\nu(2S{-}12D) + \nu(809) = 2\nu(\mathrm{LD/Rb}),$$
$$\nu(2S{-}12D) - \nu(809) = \nu(CO_2).$$

The first equation is realized at the LKB while the second one is carried out at the LPTF. For this experiment we use two-titanium-sapphire lasers. Figure 18 shows an example of the positions of the laser frequencies with respect to the FPR and FPE cavities in the case of the $2S_{1/2}$–$12D_{5/2}$ transition in hydrogen. We observe the hydrogen transitions with a first titanium-sapphire laser (TiS1). It is locked on the fringe 1 333 810 of the FPR cavity with a frequency shift due to the AOM1 (see Fig. 2). The source at 809 nm (a laser diode in an extended cavity configuration with a power of about 30 mW) and the second titanium-sapphire laser (TiS2) are frequency modulated

Table 17. Experimental determination of the 2S–12D transition frequencies in hydrogen. All the values are in MHz and we have subtracted a frequency ν_0 of 799 191 GHz. The values in bold-faced type are the ones used in the 1998 CODATA adjustment of the fundamental constants [44].

transition in hydrogen	$2S_{1/2}$–$12D_{3/2}$	$2S_{1/2}$–$12D_{5/2}$
result of the extrapolation $-\nu_0$	666.0796 (62)	683.0145 (47)
stark effect	0.0060 (49)	0.0021 (12)
black body radiation	−0.0021 (5)	−0.0021 (5)
$2S_{1/2}$ hyperfine shift	44.3892	44.3892
$\nu(2S_{1/2}$–$12D_J)-\nu_0$	**710.4727 (93)**	**727.4037 (70)**
$12D_{3/2}$–$12D_{5/2}$ splitting	16.9272	
$\nu(2S_{1/2}$–$12D_{5/2})-\nu_0$	727.3999 (93)	727.4037 (70)
mean value ($\chi^2 = 0.26$)	799 191 727.4028 (67)	

and locked on the fringes 1 237 821 and 1 333 305 of the FPE cavity. A laser diode (power of 50 mW) is injected by the LD/Rb standard and frequency doubled in a LiB_3O_5 crystal (LBO) placed in a ring cavity. This cavity is similar to the one described in reference [13]. We obtain about 10 μW in the UV. At the same time, the TiS2 laser (about 300 mW) and the source at 809 nm are summed in an other LBO crystal to obtain a second UV beam. A tracking oscillator is phase locked on the beat note between the two UV beams (frequency δ_1). A part of the 809 nm source is sent *via* one fiber to the LPTF. There, a 809 nm local laser diode is phase locked to the one at LKB. A frequency sum of this 809 nm laser diode and of an intermediate CO_2 laser in an $AgGaS_2$ crystal produces a wave at 750 nm. This wave is used to phase lock, with a frequency shift δ, a laser diode at 750 nm which is sent back to the LKB by the second optical fiber. This 750 nm laser diode is frequency shifted by $\nu(CO_2) + \delta$ with respect to the one at 809 nm. Then we use a second tracking oscillator to count the beat note (frequency δ_2) between the 750 nm laser diode and the TiS2 laser. Finally, we measure the frequency δ_3 between the two titanium-sapphire lasers. For the hydrogen measurements, the CO_2 auxiliary laser uses the P(8) line (CO_2 R(4) line for deuterium) and the frequency δ_3 is about 2.4 GHz (41.3 GHz in deuterium). The frequency δ_3 is mixed with two times the frequency which drives the AOM1, in order to eliminate the variation of the measured frequency when we scan the TiS1 frequency to observe the hydrogen lines. The 2.4 GHz frequency beat notes is detected with a fast photodiode. For deuterium, we measure the 41.3 GHz frequency with a Schottky diode. As for the hydrogen measurements of the 2S–8S/D transitions (see Sect. 4.2.2), the Schottky diode is irradiated with the two titanium-sapphire lasers and a microwave source at 13.9 GHz and we detect the beat note between the TiS1 and TiS2 lasers and the third harmonic of this microwave radiation (for this measurement we use also a tracking oscillator). Then, from the frequencies δ_1, δ_2 and δ_3, we can deduce the frequency ν(TiS1) of the TiS1 laser. Specifically, we have:

$$\nu(\mathrm{TiS1}) = \nu(\mathrm{LD/Rb}) + \frac{1}{2}\left(\nu(CO_2) + \delta + \delta_1 + \delta_2\right) + \delta_3.$$

The advantage of this scheme is that all the frequency counting is performed at the LKB.

4.3.2 Results and uncertainties

We have measured the two $2S_{1/2}(F{=}1 \text{ or } 3/2)$–$12D_{3/2}$ and $2S_{1/2}(F{=}1 \text{ or } 3/2)$–$12D_{5/2}$ two-photon transitions in hydrogen and deuterium. We have not studied the $2S_{1/2}$–$12S_{1/2}$ transition because of the low signal-to-noise ratio. For each transition, the signal is recorded for about 50 light powers (see Table 2). The extrapolated frequencies and the analysis of the data are shown in Tables 17 and 18.

For these transitions, the corrections due to the black body radiation and to the Stark effect are not negligible (several kHz), especially the Stark correction of the $2S_{1/2}$–$12D_{3/2}$ (6 kHz). In Tables 17 and 18, these transition frequencies are corrected for the hyperfine structure and compared by taking into account the theoretical value of the fine structure $12D_{3/2}$–$12D_{5/2}$. We obtain two independent values of the $2S_{1/2}$–$12D_{5/2}$ interval which are in good agreement for hydrogen and deuterium. As for the 2S–8S/D results, the final uncertainty takes into account the second order Doppler effect (1 kHz), the accuracy of the LD/Rb standard (2 kHz) and the uncertainties due to the alignment and the theoretical line shape (4 kHz and 2 kHz). Ultimately, these measurements are slightly less precise than those for the 2S–8S/D transitions, owing to the smaller signal-to-noise ratio and the larger Stark shifts.

5 Comparison of the 1S–3S and 2S–6S/D transitions

In this experiment our purpose is the determination of the 1S Lamb shift. This Lamb shift is difficult to measure, because the 1S level is isolated. Up to this experiment, all the measurements of the 1S Lamb shift have been obtained from the study of the 1S–2S two-photon transition by subtracting the 1S–2S Dirac and recoil energies from the experimental value of the 1S–2S interval [47,48]. In the most recent experiments [49,50], this subtraction is made

Table 18. Experimental determination of the 2S–12D transition frequencies in deuterium. All the values are in MHz and we have subtracted a frequency ν_0 of 799 409 GHz. The values in bold-faced type are the ones used in the 1998 CODATA adjustment of the fundamental constants [44].

transition in deuterium	$2S_{1/2}$–$12D_{3/2}$	$2S_{1/2}$–$12D_{5/2}$
result of the extrapolation $-\nu_0$	154.3925 (44)	171.3263 (45)
stark effect	0.0061 (54)	0.0011 (10)
black body radiation	−0.0021 (5)	−0.0021 (5)
$2S_{1/2}$ hyperfine shift	13.6415	13.6415
$\nu(2S_{1/2}$–$12D_J)-\nu_0$	**168.0380 (86)**	**184.9668 (68)**
$12D_{3/2}$–$12D_{5/2}$ splitting	16.9318	
$\nu(2S_{1/2}$–$12D_{5/2})-\nu_0$	184.9698 (86)	184.9668 (68)
mean value ($\chi^2 = 0.28$)	799 409 184.9676 (65)	

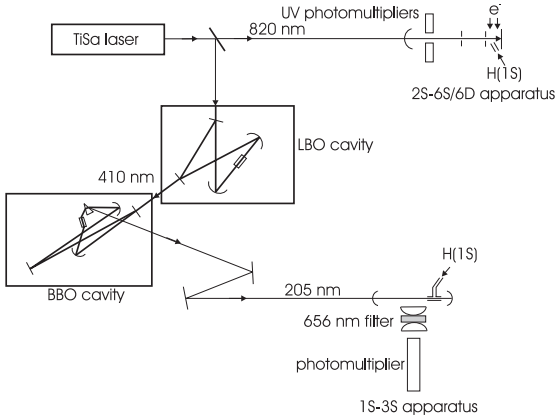

Fig. 19. Experimental setup for the frequency comparison between the 1S–3S and 2S–6S/D transitions (TiSa: titanium sapphire laser, LBO: lithium tri-borate crystal, BBO: β-barium borate crystal).

in a simple way by comparison of the 1S–2S frequency with four times the 2S–4S, 2S–4P or 2S–4D frequencies. Indeed, in the Bohr model, these frequencies lie exactly in a ratio 4:1, and the deviation from this factor is mainly due to the Lamb shifts which vary as $1/n^3$. The principle of our measurement is similar, except that we compare the 1S–3S and 2S–6S/D frequencies, which, for the same reason, are also in a ratio 4:1. This experiment has been described briefly elsewhere [9]. Here we provide some additional details and an updated analysis of the results.

5.1 The 1S–3S transition

Figure 19 shows the general scheme of the experiment. The same titanium-sapphire laser is used to observe, alternately, the 2S–6S or 2S–6D transitions at 820 nm and the 1S–3S transition at 205 nm. The 2S–6S/D apparatus is the one described in Section 2. The UV radiation at 205 nm is obtained from two successive doubling stages with a LBO crystal and a β-barium borate crystal (BBO). Both steps have been described elsewhere [13,51]. Each crystal is placed in an enhancement ring cavity. The first frequency doubling produces up to 500 mW at 410 nm for a pump power of 2.3 W at 820 nm. The second harmonic generation at 205 nm is far more challenging. To avoid rapid degradation of the faces of the BBO crystal, the second enhancement cavity is placed inside a clean chamber filled with oxygen. Moreover, the length of this enhancement cavity is modulated (modulation frequency of 15 kHz) so as to be resonant only some of the time. We work in an intermediate regime in which the UV intensity consists of 3 μs pulses at a frequency of 30 kHz. This method prevents the generation, in the ring cavity, of a counterpropagating wave at 410 nm, probably due to a photorefractive effect in the BBO crystal. This modulation produces a frequency shift, the UV frequency being upshifted (downshifted) by about 120 kHz when the length of the BBO cavity decreases (increases). In this regime, a UV power of about 1 mW (peak power) can be obtained for several hours using the same point of the crystal.

To observe the 1S–3S transition, we use a second atomic beam. Atomic hydrogen is produced by a radiofrequency discharge similar to the one described in Section 2.3.1. The discharge is off-axis with respect to the atomic beam, and linked to the vacuum chamber by a 9 cm length of Teflon tube. The atomic hydrogen flows through a Teflon nozzle (3 cm long, 3 mm in diameter) into the vacuum chamber which is evacuated by an oil diffusion pump (Alcatel 6250). Under running conditions, the pressures in the discharge tube and the vacuum chamber are 0.4 mbar and 9×10^{-5} mbar respectively. With the method described in reference [52], we have measured the angular width of the profile of the effusive atomic beam to be about 8° (full width at the half maximum). By comparison with a previous version of the experiment where the discharge was on the axis of the atomic beam (there was only the Teflon nozzle), we have also found that the atomic flux is reduced by about a factor 4. This effect shows that the recombination of the hydrogen atoms in the Teflon tube is significant. The atomic beam is carefully delimited by two diaphragms (diameter of 2 mm and 3 mm successively) to eliminate the stray light coming from the hydrogen discharge. The atomic beam is also placed inside a linear

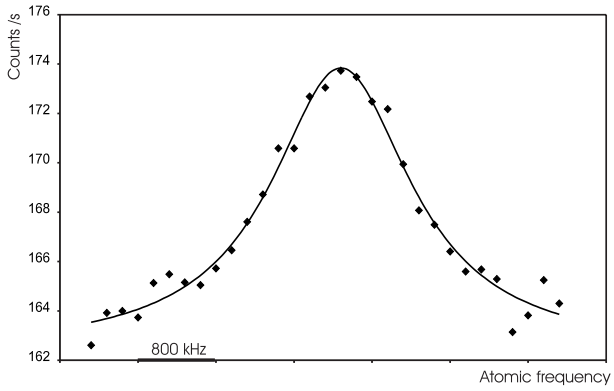

Fig. 20. Spectrum of the $1S_{1/2}(F = 1)$–$3S_{1/2}(F = 1)$ transition detected by Balmer-α fluorescence. The total acquisition time is about 14 hours. The signal is fitted with a Lorentzian curve (solid).

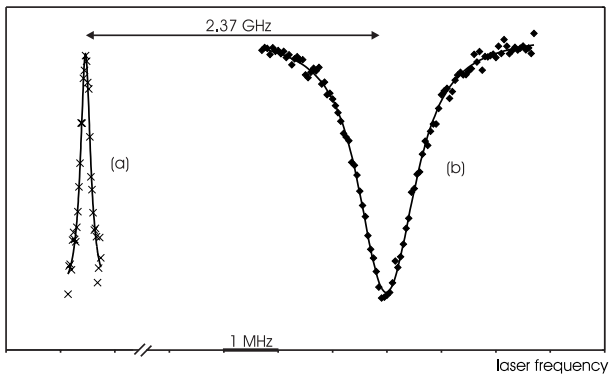

Fig. 21. Hydrogen two-photon spectra. (a) $1S_{1/2}(F = 1)$–$3S_{1/2}(F = 1)$ transition. (b) $2S_{1/2}(F = 1)$–$6D_{5/2}$ transition. The two signals are shifted by about 2.37 GHz in terms of laser frequency at 820 nm.

buildup cavity formed by two spherical mirrors (radius of curvature 25 cm). The UV beam emerging from the BBO crystal is corrected for astigmatism with a spherical lens (focal length 87 mm) and a cylindrical lens (focal length 290 mm) and mode matched into the cavity with two more lenses. Inside the cavity, the UV power is typically 10 mW and the UV beam is focused at a distance of 12 cm from the Teflon nozzle with a waist of about 48 μm. At this distance, we estimate the density of hydrogen atoms to be about 3×10^{10} atoms/cm^3. The two cavity mirrors are mounted on PZT stacks and the length of the cavity is locked to the UV frequency so that successive UV pulses have the same intensity inside the cavity. In these conditions, the frequency shifts of two successive UV pulses cancel each other and the residual frequency shift is estimated to be less than 3 kHz. The two-photon transition is detected by monitoring the Balmer-α fluorescence due to the radiative decay 3S–2P. This fluorescence is collected with a spherical mirror and a $f/0.5$ aspheric lens system, selected with an interference filter and detected with a cooled photomultiplier (EMI 9658R).

The data acquisition is similar to the one described in Section 2.4. Each scan is divided in 31 frequency points. For each point, the photomultiplier signal is counted during 1 s and we make 10 scans of the line to achieve a 7 minute run. As the signal-to-noise ratio is small, we take the mean of several runs to obtain an observable signal. Figure 20 shows the mean of 102 runs. The total background is about 160 counts/s and the 1S–3S signal 10 counts/s. In Figure 20, the signal is fitted with a Lorentzian curve. The observed line width (1.7 MHz in terms of atomic frequency) is mainly due to the natural width of the 3S level (1 MHz), transit time broadening (200 kHz) and broadening due to the modulation of the UV light (about 500 kHz). We can compare the signal amplitude with a theoretical estimate. The two-photon transition probability Γ_g is given by equation (9). As the value of the matrix element $\langle 3S\,|Q_{\rm tp}|\,1S\rangle$ of the two-photon operator is 2.14 in atomic units [53], we obtain for a UV power of 10 mW: $\Gamma_g = 2\times10^{-2}$ s^{-1}. If we take into account the effective linewidth (1.7 MHz), the atomic density in front of the photomultiplier (3×10^{10} atoms/cm^3), the observation length (12 mm because of the transmission of the interference filter), the detection solid angle ($\Omega/4\pi = 0.24$), the transmission of the detection optics (about 66%), the photomultiplier quantum efficiency (8%), the population of the $F = 1$ hyperfine level (3/4) and the modulation of the UV light (reduction of the excitation time by a factor 0.066), we estimate the signal to be about 20 counts/s. This value is in fair agreement with the experiment if we consider the uncertainties in the UV power and the atomic density.

5.2 Comparison of the 1S–3S and 2S–6S/D frequencies

We have compared the $1S_{1/2}$–$3S_{1/2}$ frequencies with those of the $2S_{1/2}$–$6D_{5/2}$ and $2S_{1/2}$–$6S_{1/2}$ transitions. To do this, we have measured alternately the 1S–3S and 2S–6S/D line positions with respect to the fringes 1 219 477 (transition $1S_{1/2}$–$3S_{1/2}$) and 1 219 485 (transition $2S_{1/2}$–$6D_{5/2}$) or 1 219 484 (transition $2S_{1/2}$–$6S_{1/2}$) of our very stable FPR cavity. For the first comparison, we collected the data for the $2S_{1/2}$–$6D_{5/2}$ transition (1 day), the $1S_{1/2}$–$3S_{1/2}$ (3 days), then $2S_{1/2}$–$6D_{5/2}$ once again (2 days). The procedure was similar for the $2S_{1/2}$–$6S_{1/2}$ transition, but, because of its lower intensity, longer acquisition times were required (4, 3 and 4 days respectively). Figure 21 shows, on the same frequency scale, the recordings of the $1S_{1/2}$–$3S_{1/2}$ and $2S_{1/2}$–$6D_{5/2}$ lines. As the 2S–6S/D linewidth is larger than the 1S–3S one, the accuracy is mainly limited by the uncertainty in the 2S–6S/D line positions.

The results are given in Table 19. For the 2S–6S/D transitions, we have used our updated analysis of the data: the second-order Doppler effect and the 6D hyperfine structure are included in the theoretical line shape. The quoted uncertainties of the second row of the table (8.8 kHz and 20 kHz for each measurement) are mainly due to the uncertainties in the positions of the 1S–3S line

Table 19. Comparison between the $1S_{1/2}$–$3S_{1/2}$ and $2S_{1/2}$–$6D_{5/2}/6S_{1/2}$ frequencies. All the values are in MHz. The values in bold-faced type are the ones used in the 1998 CODATA adjustment of the fundamental constants [44].

comparison with	$2S_{1/2}$–$6D_{5/2}$	$2S_{1/2}$–$6S_{1/2}$
laser frequency splitting	2370.1140 (44)	2120.188 (10)
laser frequency splitting ×2	4740.2280 (88)	4240.377 (20)
1S–3S second-order Doppler effect	−0.0310 (25)	−0.0310 (25)
hyperfine structure corrections	−41.0981	−42.7421
ν(2S–6S/D) − ν(1S–3S)/4	**4699.099 (11)**	**4197.604 (21)**
$6S_{1/2}$–$6D_{5/2}$ splitting		501.5051
$\nu(2S_{1/2}–6D_{5/2}) - \nu$(1S–3S)/4	4699.099 (11)	4699.109 (21)
mean value	4699.1006 (98)	

(4.7 kHz and 6 kHz for each measurement) and of the 2S–6D or 2S–6S lines (7.1 kHz and 19 kHz). For the 1S atomic beam, the velocity distribution is that of a thermal beam, *i.e.* $f(v) \sim v^3 \exp\left(-v^2/2\sigma^2\right)$ and the second-order Doppler shift of the 1S–3S line is $-3/2(\sigma/c)^2\nu_{1S-3S}$ (see Eq. (2)). The analysis of the features of the metastable atomic beam shows that the heating due to the discharge is typically 30 K. As the two discharges of the two atomic beams are of identical design, we can assume that the temperature of the beam is in the range 280–330 K and we obtain a second-order Doppler shift of −124(10) kHz for the 1S–3S transition in terms of atomic frequency, *i.e.* −31.0(2.5) kHz for the comparison with the 2S–6S/D frequencies. Because of the 1S and 3S hyperfine structures, there is a quadratic Zeeman effect of the $F = 1, m_F = 0$ sublevels. For the 1S–3S line this effect introduces a mean shift of 11.9 kHz/G^2 (in terms of atomic frequency). In our experiment, the Earth's magnetic field is about 260 mG and the Zeeman shift of the 1S–3S transition 800 Hz. We have neglected this effect and several other small effects: the shifts due to the black body radiation (see Tab. 8), the residual Stark shifts (smaller than 300 Hz for the 2S–6S/D transition) and the light shift of the 1S–3S transition. For this transition, the light shift coefficients β_i (see Eq. (11)) are −6.445 and 20.926 (atomic units) for the 1S and 3S level respectively [19]. With a UV power of 10 mW, the light shift is about 740 Hz for an atom at the center of the laser beam. As previously, the final uncertainties (11 kHz and 21 kHz for the two measurements, see Tab. 19) take into account the uncertainty of the second-order Doppler effect of the 2S–6S/D lines (2 kHz), and the uncertainties due to the alignment and the theoretical line shape (4 kHz and 2 kHz).

Finally, if we use the theoretical value of the $6S_{1/2}$–$6D_{5/2}$ splitting, we can compare the two measurements. We obtain two independent values of the frequency difference $\nu(2S_{1/2}–6D_{5/2}) - \nu(1S–3S)/4$ which are in fair agreement. By comparison with the results published previously [9], these values are shifted by 6 kHz and −3.7 kHz for the $2S_{1/2}$–$6D_{5/2}$ and $2S_{1/2}$–$6S_{1/2}$ measurements because of the new theoretical line shape. Finally we obtain an uncertainty of 9.8 kHz for the difference $\nu(2S_{1/2}–6D_{5/2}) - \nu(1S–3S)/4$.

6 Determination of the Rydberg constant and Lamb shifts

6.1 Method and analysis of the data

6.1.1 Theoretical background

The aim of this section is to extract from our measurements the values of Rydberg constant and Lamb shifts. More details of the theory of atomic hydrogen can be found in the review articles [38–40]. The hydrogen level energy is conventionally expressed as the sum of three terms: the energy given by the Dirac equation for a particle with the reduced mass, the first relativistic correction due to the recoil of the proton, and the Lamb shift. The energy $E_{\rm H}(nLJ)$ of the level $|nLJ\rangle$ of hydrogen is:

$$E_{\rm H}(nLJ) = d_{\rm H}(nLJ)hcR_\infty + r_{\rm H}(n)hcR_\infty + hL_{\rm H}(nLJ) \quad (35)$$

where $d_{\rm H}(nLJ)hcR_\infty$ and $r_{\rm H}(nLJ)hcR_\infty$ describe the Dirac and recoil energies. The coefficients $d_{\rm H}(nLJ)$ and $r_{\rm H}(n)$ can be expressed exactly as a function of the fine structure constant α and the electron to proton mass ratio $m_{\rm e}/m_{\rm p}$. Moreover, the coefficient $r_{\rm H}(n)$ does not depend on the quantum numbers L and J [20]. The Lamb shift $L_{\rm H}(nLJ)$ is expressed in terms of frequency. It contains all the theoretical corrections, *i.e.* the QED corrections, the other relativistic corrections due to the proton recoil and the effect of the proton charge distribution. For deuterium, the energy $E_{\rm D}(nLJ)$ is given by a similar equation with the subscripts D. Equation (35) shows that, to extract the Rydberg constant from our measurements, we need to know the Lamb shifts. For the upper levels of the transitions, we can use the theoretical values of the Lamb shift (see Tab. 14), because the theoretical uncertainties (only a few hundred hertz) are far smaller than those of our measurements (typically 6 kHz). On the other hand, for the 1S and 2S levels, this is not the case. The one-loop QED corrections are now calculated with an accuracy of 1 Hz [54]. By contrast, for the calculations of the higher order terms, the QED uncertainties are typically 5 kHz and 40 kHz for the 2S and 1S levels [55–57]. Moreover, the disagreement between the two determinations

of the charge radius of the proton ($r_p = 0.805(11)$ fm [58] and $r_p = 0.862(12)$ fm [41]) corresponds to a difference of 18 kHz and 149 kHz respectively for the 2S and 1S Lamb shifts. Consequently, in our data analysis, we shall consider that the 1S and 2S Lamb shifts are unknowns to be determined by the experiment. Nevertheless, since several terms of the Lamb shift calculations vary with the principal quantum number exactly as $1/n^3$ (for instance the effect of the charge distribution of the nucleus), the deviation from this scaling law as been calculated precisely by Karshenboim [59]. For the 1S and 2S levels of hydrogen and deuterium the results are:

$$L_H(1S_{1/2}) - 8L_H(2S_{1/2}) = -187.232(5)\ \text{MHz} \quad (36)$$

$$L_D(1S_{1/2}) - 8L_D(2S_{1/2}) = -187.225(5)\ \text{MHz} \quad (37)$$

as one might expect, there are similar equations for the other $n\mathrm{S}_{1/2}$ levels.

6.1.2 Experimental data

To determine the Rydberg constant and the Lamb shifts, we use the mean values of the frequencies $\nu_A(2S_{1/2}–nD_{5/2})$ (A = H or D and n = 8 or 12) and of the frequency difference $\nu_H(2S_{1/2}–6D_{5/2}) - \nu_H(1S_{1/2}–3S_{1/2})/4$ which are given at the end of the Tables 15–19. We have introduced the subscripts H and D to distinguish the hydrogen and deuterium cases. If we define the coefficient $a_A(2S_{1/2}–nD_{5/2}) = d_A(nD_{5/2}) + r_A(nD_{5/2}) - d_A(2S_{1/2}) - r_A(2S_{1/2})$ we deduce from our experimental results five equations:

$$\nu_A(2S_{1/2}–nD_{5/2}) = a_A(2S_{1/2}–nD_{5/2})cR_\infty + L_A(nD_{5/2}) - L_A(2S_{1/2}) \quad \text{(4 equations)}. \quad (38)$$

And we obtain from the 1S–3S and 2S–6S/D comparison:

$$\nu_H(2S_{1/2}–6D_{5/2}) - \frac{1}{4}\nu_H(1S_{1/2}–3S_{1/2}) = \left[a_H(2S_{1/2}–6D_{5/2}) - \frac{1}{4}a_H(1S_{1/2}–3S_{1/2})\right] cR_\infty + L_H(6D_{5/2}) - L_H(2S_{1/2}) - \frac{1}{4}\left(L_H(3S_{1/2}) - L_H(1S_{1/2})\right). \quad (39)$$

We will use also several other precise measurements in hydrogen and deuterium, at first the measurements of the 2S Lamb shift in hydrogen. This Lamb shift (in fact the difference between the $2S_{1/2}$ and $2P_{1/2}$ Lamb shifts) is deduced from radiofrequency measurements of the $2P_{1/2}$–$2S_{1/2}$ splitting, the first by Lamb and Retherford [60]. The most precise direct determination of this splitting is the one by Lundeen and Pipkin (1 057.845(9) MHz [61]). We have also used two other indirect determinations deduced from the $2S_{1/2}$–$2P_{3/2}$ splitting (1 057.842(12) MHz [62,63]) and obtained by the anisotropy method (1 057.852(15) MHz [64]). From the weighted mean value of these three results (1 057.8454(65) MHz) and the theoretical value of the $2P_{1/2}$ Lamb shift (−12.835 99(8) MHz [63]) we deduce the $2S_{1/2}$ Lamb shift:

$$L_H(2S_{1/2}) = 1\,045.009\,4(65)\ \text{MHz}. \quad (40)$$

We have not taken into account the determination of Pal'chikov *et al.* (1 057.8514(19) MHz [65]) who measured in fact the ratio between the $2S_{1/2}$ Lamb shift and the natural width of the $2P_{1/2}$ level. Since there is an ongoing discussion about the theoretical value of this natural width [66,67], we have not used this result.

The frequency and the isotope shift of the 1S–2S transition have been measured very accurately by Hänsch and coworkers [2,3]. Their results provide us with equations:

$$\nu_H(1S_{1/2}–2S_{1/2}) = a_H(1S_{1/2}–2S_{1/2})cR_\infty + L_H(2S_{1/2}) - L_H(1S_{1/2}), \quad (41)$$

$$\nu_D(1S_{1/2}–2S_{1/2}) - \nu_H(1S_{1/2}–2S_{1/2}) = \left[a_D(1S_{1/2}–2S_{1/2}) - a_H(1S_{1/2}–2S_{1/2})\right] cR_\infty + L_D(2S_{1/2}) - L_H(2S_{1/2}) - L_D(1S_{1/2}) + L_H(1S_{1/2}). \quad (42)$$

Lastly, we will use also the measurements of the $1S_{1/2}$ Lamb shift made by comparison of the 1S–2S frequency with the 2S–4S/D frequencies [42,49] or with the 2S–4P frequencies [50]. If we use the theoretical values of the Lamb shifts for the $n = 4$ levels, the analysis of these data gives two experimental values of the linear combination of the Lamb shifts:

$$L_H(1S_{1/2}) - 5L_H(2S_{1/2}) = 2\,947.831(37)\ \text{MHz} \quad (1S–2S \text{ and } 2S–4S/D \text{ comparison}), \quad (43)$$

$$L_H(1S_{1/2}) - 5L_H(2S_{1/2}) = 2\,947.787(34)\ \text{MHz} \quad (1S–2S \text{ and } 2S–4P \text{ comparison}). \quad (44)$$

These two measurements are in fair agreement with each other.

To conclude, we obtain a set of 12 equations where the 5 unknowns are the Rydberg constant and the Lamb shifts of the 1S and 2S levels in hydrogen and deuterium: 2 theoretical equations (36, 37), 5 equations given by our experimental results (38, 39) and 5 equations which resume the accurate measurements made in hydrogen or deuterium by several other groups (40–44). This set of equations give us the possibility, with least squares procedures, to extract the Rydberg constant and the Lamb shifts by different ways. We present several approaches below. For these calculations, we use the value of the fine structure constant given by the last adjustment of the fundamental constants $\alpha^{-1} = 137.035\,999\,76(50)$ [44]. This choice is justified because, in this adjustment, the hydrogen measurements have no significant influence on the determination of the fine structure constant. For the proton-to-electron and deuteron-to-proton mass ratios, we use the values taken from references [68,69]: $m_p/m_e = 1\,836.152\,666\,5(40)$ and $m_d/m_p = 1.999\,007\,501\,3(14)$.

Table 20. Determination of the Rydberg constant.

method and transitions involved	equations	$(R_\infty - 109\,737)$ cm^{-1}
determination of R_∞ from the 2S–nD and 2S–2P measurements		
2S–2P and 2S–8S/D in hydrogen	(38, 40)	0.315 6861(13)
2S–2P and 2S–12D in hydrogen	(38, 40)	0.315 6848(13)
2S–2P, 2S–8S/D and 2S–12D in hydrogen	(38, 40)	0.315 6855(11)
determination of R_∞ from linear combination of optical frequencies measurements		
2S–8S/D, 1S–2S and $1/n^3$ law in hydrogen	(36, 38, 41)	0.315 6865(16)
2S–12D, 1S–2S and $1/n^3$ law in hydrogen	(36, 38, 41)	0.315 6842(17)
2S–8S/D, 2S–12D, 1S–2S and $1/n^3$ law in hydrogen	(36, 38, 41)	0.315 6854(13)
2S–8S/D, 2S–12D, 1S–2S and $1/n^3$ law in deuterium	(37, 38, 41, 42)	0.315 6854(12)
2S–8S/D, 2S–12D, 1S–2S and $1/n^3$ law in hydrogen and deuterium	(36–38, 41, 42)	0.315 6854(10)
general least squares adjustment in hydrogen and deuterium		
2S–2P, 2S–8S/D, 2S–12D, 1S–2S and $1/n^3$ law	(36–44)	0.315 685 50(84)

6.2 Rydberg constant

We can extract the Rydberg constant from only our results by considering the $8D_{5/2}$–$12D_{5/2}$ splitting, which is obtained by difference between our $2S_{1/2}$–$8D_{5/2}$ and $2S_{1/2}$–$12D_{5/2}$ measurements. Nevertheless, since this splitting is small (about 30 THz), the relative accuracy of this method is only 2×10^{-10}. A first precise method is to use the experimental determination of the $2S_{1/2}$ Lamb shift in hydrogen (Eq. (40)). The first part of Table 20 gives the values of the Rydberg constant deduced from our $2S_{1/2}$–$8D_{5/2}$ and $2S_{1/2}$–$12D_{5/2}$ measurements in hydrogen. These two values have a similar precision and are in an acceptable agreement (they differ by about 1 standard deviation). This agreement shows that the corrections due to the Stark effect are well analyzed (these corrections are about 10 times larger for the 12D than for the 8D levels, see Tab. 12). Table 20 gives the average of these results ($R_\infty = 109\,737.315\,685\,5(11)$ cm^{-1}). The relative uncertainty (about 10^{-11}) comes from the optical frequency measurements (6.1×10^{-12}), the $2S_{1/2}$ Lamb shift (8.3×10^{-12}) and the proton-to-electron mass ratio (1.2×10^{-12}). The uncertainty due to the fine structure constant is negligible (1.3×10^{-13}). This result is the most precise if we make no theoretical assumptions concerning the $1S_{1/2}$ and the $2S_{1/2}$ Lamb shifts. Unfortunately, this method is not appropriate for deuterium, because, for this isotope, no comparably accurate determination of the $2S_{1/2}$ Lamb shift has been performed.

If we use the $1/n^3$ scaling law for the Lamb shifts (Eqs. (36, 37)), we can form the linear combination of the $1S_{1/2}$–$2S_{1/2}$ and $2S_{1/2}$–$nD_{5/2}$ frequencies:

$$7\nu_{\rm H}(2S_{1/2}-nD_{5/2}) - \nu_{\rm H}(1S_{1/2}-2S_{1/2}).$$

In this way, we can eliminate from the equations (38, 41) the Lamb shift combination $L_{\rm H}(1S_{1/2}) - 8L_{\rm H}(2S_{1/2})$ (Eq. (36)) and we deduce the Rydberg constant without the microwave measurements of the $2S_{1/2}$ Lamb shift. Moreover, this method is applicable to both hydrogen and deuterium. The results are given in the second part of Table 20. The values obtained for hydrogen and deuterium are in perfect agreement. If we use all the precise optical frequency measurements in hydrogen and deuterium (transitions $1S_{1/2}$–$2S_{1/2}$, $2S_{1/2}$–$8D_{5/2}$ and $2S_{1/2}$–$12D_{5/2}$), we obtain a value of R_∞ more precise than the previous ones ($R_\infty = 109\,737.315\,685\,4(10)$ cm^{-1}). This value is also in perfect agreement with the one deduced *via* the measurements of the $2S_{1/2}$ Lamb shift.

To make an average of these different determinations of R_∞, we have performed a least squares adjustement which takes into account all the precise measurements described by the equations (36–44): the measurements of the $2S_{1/2}$ Lamb shift, the optical frequency measurements of the 1S–2S and 2S–nD transitions in hydrogen and deuterium, and also the measurements of the 1S Lamb shift which will be described in Section 6.3. This result ($R_\infty = 109\,737.315\,685\,50(84)$ cm^{-1}) is similar to the one of the 1998 adjustment of the fundamental constant [44], with a relative uncertainty of 7.7×10^{-12}. By comparison with the 1986 adjustment [70], the uncertainty is reduced by a factor of about 150. Figure 22 compares the recent determinations of the Rydberg constant and shows the different steps of this improvement since 1986.

The values of Table 20 are slightly different from the ones published previously [8], because for the fine structure constant α we had used the value of the 1986 CODATA adjustment, which differs from the new value by about 7.5×10^{-8} [70]. To obtain these results, we have chosen to leave out our first determination of the $2S_{1/2}$–$8D_{5/2}$ frequency (see Tab. 13), because this measurement has no significant bearing upon the final result: if we included this value, the uncertainty in R_∞ would be reduced to only 83×10^{-8} cm^{-1}.

6.3 Lamb shifts

We can deduce the $1S_{1/2}$ Lamb shift from the comparison of the $1S_{1/2}$–$3S_{1/2}$ and $2S_{1/2}$–$6D_{5/2}$ frequencies

Table 21. Determination of the $1S_{1/2}$ Lamb shift in hydrogen.

method and transitions involved	equations	$L_H(1S_{1/2})$ (MHz)
comparison of transition frequencies lying in a ratio 4:1		
2S–2P, 1S–3S and 2S–6S/D	(39, 40)	8 172.825(47)
2S–2P, 1S–2S and 2S–4S/D	(43, 40)	8 172.878(51)
2S–2P, 1S–2S and 2S–4P	(44, 40)	8 172.834(48)
comparison of the 1S–2S and 2S–nD frequencies using the $2S_{1/2}$ Lamb shift		
2S–2P, 1S–2S and 2S–8S/D	(38, 40, 41)	8 172.854(33)
2S–2P, 1S–2S and 2S–12D	(38, 40, 41)	8 172.825(34)
2S–2P, 1S–2S, 2S–8S/D and 2S–12D	(38, 40, 41)	8 172.840(31)
comparison of the 1S–2S and 2S–nD frequencies using the $1/n^3$ scaling law		
2S–8S/D, 2S–12D, 1S–2S and $1/n^3$ law in hydrogen	(36, 38, 41)	8 172.837(32)
2S–8S/D, 2S–12D, 1S–2S and $1/n^3$ law in hydrogen and deuterium	(36–38, 41, 42)	8 172.837(26)
general least squares adjustment in hydrogen and deuterium		
2S–2P, 2S–8S/D, 2S–12D, 1S–2S and $1/n^3$ law	(36–44)	8 172.840(22)
theory $r_p = 0.862(12)$ fm [56]		8 172.731(40)
theory $r_p = 0.805(11)$ fm [56]		8 172.582(40)

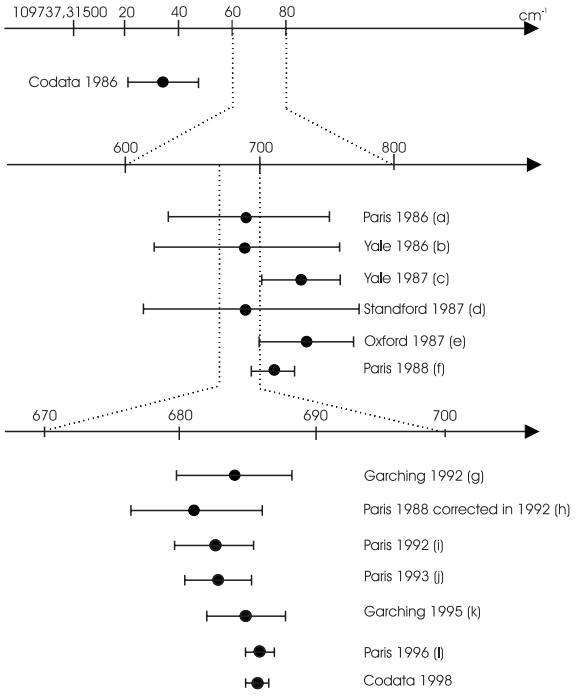

Fig. 22. Comparison of various determinations of the Rydberg constant since the 1986 adjustment of the fundamental constants; Codata 1986 [70], a [71], b [72], c [73], d [74], e [48], f [75], g [76], h: reference [75] corrected for the new measurement of the He–Ne/I_2 standard laser [33], i [4], j [5], k [42], l [6], Codata 1998 [44].

(see Eq. (39)). The value of the term $[a_H(2S_{1/2}-6D_{5/2}) - a_H(1S_{1/2}-3S_{1/2})/4]cR_\infty$ is 3 778.5887 MHz. If we use the theoretical values of the $2S_{1/2}$ and $6D_{5/2}$ Lamb shift, we obtain the linear combination of the $1S_{1/2}$ and $2S_{1/2}$ Lamb shifts:

$$L_H(1S_{1/2}) - 4L_H(2S_{1/2}) = 3\,992.787(39) \text{ MHz}. \quad (45)$$

Finally, thanks to the experimental value of the $2S_{1/2}$ Lamb shift (Eq. (40)) we deduce the value $L_H(1S_{1/2}) = 8\,172.825(47)$ MHz. This value differs from the one published previously by 27 kHz. This is due to a different value of the $2S_{1/2}$ Lamb shift (10 kHz) and to our new theoretical line shape (17 kHz). This result is compared in the first part of Table 21 with the determinations obtained by comparison of the 1S–2S and 2S–4S/D or 2S–4P frequencies (Eqs. (43, 44); with respect to references [42, 50], these two values are updated by taking into account the different values of the $2S_{1/2}$ Lamb shift and of the fine structure constant). The three results have a similar precision and are in good agreement.

Another way to obtain the $1S_{1/2}$ Lamb shift is to use the precise optical frequency measurements of the $1S_{1/2}$–$2S_{1/2}$ and $2S_{1/2}$–$nD_{5/2}$ transitions. A first method uses the experimental value of the $2S_{1/2}$ Lamb shift (Eq. (40)) to extract R_∞ from the $2S_{1/2}$–$nD_{5/2}$ splitting (see the first part of Tab. 20). Then the $1S_{1/2}$ Lamb shift is deduced from the $1S_{1/2}$–$2S_{1/2}$ frequency. The results are given in the second part of Table 21. The final result ($L_H(1S_{1/2}) = 8\,172.840(31)$ MHz) is more precise than the precedent ones because of the very high accuracy of the optical frequency measurements. The 31 kHz uncertainty is due to the optical frequency measurements (15 kHz) and, mainly, to the measurement of the $2S_{1/2}$ Lamb shift (27 kHz). In a second method, we can avoid this limitation by using the $1/n^3$ scaling law of the Lamb shift. The values obtained by this way are slightly more precise (see the third part of Tab. 21). Moreover, this method provides the $2S_{1/2}$ Lamb shift and is reliable in the case of deuterium. Finally, we give the result of the general

Table 22. Determination of the $1S_{1/2}$ Lamb shift in deuterium.

method and transitions involved	equations	$L_D(1S_{1/2})$ (MHz)
comparison of transition frequencies lying in a ratio 4:1		
1S–2S, 2S–4S/D and theoretical value of $L_D(2S_{1/2})$ [42]		8 183.807(78)
comparison of the 1S–2S and 2S–nD frequencies using the $1/n^3$ scaling law		
2S–8S/D, 2S–12D, 1S–2S and $1/n^3$ law in deuterium	(37, 38, 41, 42)	8 183.968(31)
2S–8S/D, 2S–12D, 1S–2S and $1/n^3$ law in hydrogen and deuterium	(36–38, 41, 42)	8 183.967(26)
general least squares adjustment in hydrogen and deuterium		
2S–2P, 2S–8S/D, 2S–12D, 1S–2S and $1/n^3$ law	(36–44)	8 183.970(22)

Table 23. Determination of the $2S_{1/2}$ Lamb shift in hydrogen.

method and transitions involved	equations	$\nu_H(2S_{1/2}-2P_{1/2})$ (MHz)
direct measurement of the $2S_{1/2}$–$2P_{1/2}$ splitting		
$2S_{1/2}$–$2P_{1/2}$, Newton *et al.* [77]		1 057.862(20)
$2S_{1/2}$–$2P_{1/2}$, Lundeen *et al.* [61]		1 057.845(9)
$2S_{1/2}$–$2P_{3/2}$, Hagley *et al.* [62,63]		1 057.842(12)
2S–2P, Wijngaarden et al. [64]		1 057.852(15)
comparison of transition frequencies lying in a ratio 4:1		
1S–3S, 2S–6S/D and $1/n^3$ scaling law	(36, 39)	1 057.841(10)
1S–2S, 2S–4S/D and $1/n^3$ scaling law	(36, 43)	1 057.857(12)
1S–2S, 2S–4P and $1/n^3$ scaling law	(36, 44)	1 057.842(11)
comparison of the 1S–2S and 2S–nD frequencies using the $1/n^3$ scaling law		
2S–8S/D, 2S–12D, 1S–2S and $1/n^3$ law in hydrogen	(36, 38, 41)	1 057.8446(42)
2S–8S/D, 2S–12D, 1S–2S and $1/n^3$ law in hydrogen and deuterium	(36–38, 41, 42)	1 057.8447(34)
general least squares adjustment in hydrogen and deuterium		
2S–2P, 2S–8S/D, 2S–12D, 1S–2S and $1/n^3$ law	(36–44)	1 057.8450(29)
theory $r_p = 0.862(12)$ fm [56]		1 057.836(6)
theory $r_p = 0.805(11)$ fm [56]		1 057.812(6)

adjustment ($L_H(1S_{1/2}) = 8\,172.840(22)$ MHz) with a relative uncertainty of 2.7×10^{-6}.

Table 22 gives the results for the $1S_{1/2}$ Lamb shift in deuterium. First, we recall the value of reference [42] which was obtained by comparison of the 1S–2S and 2S–4S/D frequencies, but which used the theoretical value of the $2S_{1/2}$ Lamb shift. Afterwards, we give the results of the comparison of the 1S–2S and 2S–nD frequencies and we conclude with the general least square adjustment in hydrogen and deuterium. This last value ($L_D(1S_{1/2}) = 8\,183.970(22)$ MHz) has the same uncertainty as that for hydrogen.

Several values of the $2S_{1/2}$ Lamb shift in hydrogen and deuterium are given in Tables 23 and 24. The first part of these tables displays the determinations deduced from the 2S–2P splitting by microwave spectroscopy or by level crossing or anisotropy methods [61,62,64,77,78]. For hydrogen, the combination of the equations (43, 44, 45) with the $1/n^3$ scaling law of the Lamb shift (Eq. (36)) yields three determinations of the $2S_{1/2}$ Lamb shift (second part of Tab. 23) with a precision equivalent to that of the direct measurements. For deuterium, a first value of the $2S_{1/2}$ Lamb shift is deduced from the isotope shift of the $2S_{1/2}$–$8D_{5/2}$ and $2S_{1/2}$–$12D_{5/2}$ transitions. These isotope shifts are mainly a mass effect. Thanks to the precise determination of the mass ratios m_p/m_e and m_d/m_p, the uncertainty in the mass effect is only 0.5 kHz. Then, from these isotope shifts, we deduce the difference between the $2S_{1/2}$ Lamb shift in deuterium and hydrogen. By using the experimental value of the $2S_{1/2}$ Lamb shift in hydrogen, we obtain finally the $2S_{1/2}$ Lamb shift in deuterium (second part of Tab. 24). To obtain the $2S_{1/2}$–$2P_{1/2}$ splitting, we use the theoretical value of the $2P_{1/2}$ Lamb shift ($L_D(2P_{1/2}) = -12.8350(3)$ MHz). These results are in very good agreement with the first measurement of Cosens [78].

Next we give the values deduced from the 1S–2S and 2S–nD optical frequency measurements. These results for the $2S_{1/2}$ Lamb shift ($L_H(2S_{1/2}) = 1\,057.8447(34)$ MHz and $L_D(2S_{1/2}) = 1\,059.2338(34)$ MHz) are independent and more precise than the direct determinations made by microwave spectroscopy. Lastly, we make

Table 24. Determination of the $2S_{1/2}$ Lamb shift in deuterium.

method and transitions involved	equations	$\nu_D(2S_{1/2}-2P_{1/2})$ (MHz)
direct measurement of the $2S_{1/2}$–$2P_{1/2}$ splitting		
$2S_{1/2}$–$2P_{1/2}$, Cosens [78]		1 059.240(33)
determination from the $2S_{1/2}$–$nD_{5/2}$ isotope shift		
2S–2P in H and 2S–8S/D in H and D	(38, 40)	1 059.234(10)
2S–2P in H and 2S–12D in H and D	(38, 40)	1 059.235(11)
2S–2P in H, 2S–8S/D and 2S–12D in H and D	(38, 40)	1 059.234(8)
comparison of the 1S–2S and 2S–nD frequencies using the $1/n^3$ scaling law		
2S–8S/D, 2S–12D, 1S–2S and $1/n^3$ law in deuterium	(37, 38, 41, 42)	1 059.234(4)
2S–8S/D, 2S–12D, 1S–2S and $1/n^3$ law in hydrogen and deuterium	(36–38, 41, 42)	1 059.2338(34)
general least squares adjustment in hydrogen and deuterium		
2S–2P, 2S–8S/D, 2S–12D, 1S–2S and $1/n^3$ law	(36–44)	1 059.2341(29)

an average of all these determinations: the results ($L_H(2S_{1/2})$ = 1 057.8450(29) MHz and $L_D(2S_{1/2})$ = 1 059.2341(29) MHz), with an uncertainty of 2.9 kHz, are the most precise to date.

For hydrogen, we compare the values of the $1S_{1/2}$ and $2S_{1/2}$ Lamb shift with theory [56] (see Tabs. 21 and 23). There is a large discrepancy, which varies from 2.4 to 5.6 standard deviations according to which value of the proton charge radius one adopts (r_p = 0.862(12) fm [41] or r_p = 0.805(11) fm [58]). This discrepancy is perhaps due to the calculation of the two-loop corrections [57]. Conversely, if we believe the calculations of the reference [56], we can deduce the radius of the proton charge distribution r_p = 0.901(16) fm.

6.4 Proton-to-electron mass ratio

In a first approximation, the isotope shift of an optical transition is proportional to $(m_e/m_p)(1 - m_p/m_d)cR_\infty$. Since the deuteron-to-proton mass ratio is known with a high accuracy (relative uncertainty of 7×10^{-10}), we could deduce the proton-to-electron mass ratio from the value of the isotope shift. In actual fact, this method is not reliable, because the corrections due to the charge distribution of the proton and deuteron are not well known. To avoid this difficulty, we consider the isotope shift Δ_{H-D} on the linear frequency combination $7\nu(2S_{1/2}-nD_{5/2}) - \nu(1S_{1/2}-2S_{1/2})$, where the Lamb shifts are eliminated using equations (36, 37). From the measurements of the $1S_{1/2}$–$2S_{1/2}$, $2S_{1/2}$–$8D_{5/2}$ and $2S_{1/2}$–$12D_{5/2}$ frequencies, we deduce the values:

$$\Delta_{H-D}(n = 8) = 796\,844.536(50) \text{ MHz}$$

$$\Delta_{H-D}(n = 12) = 851\,208.619(59) \text{ MHz}$$

where the uncertainties are mainly due to the measurements of the $2S_{1/2}$–$nD_{5/2}$ frequencies.

To sum up, we can obtain two independent values of the proton-to-electron mass ratio which are given in Table 25. The weighted mean value is m_p/m_e = 1 836.152 667(85) with a relative uncertainty of 4.6×10^{-8}. This value is in perfect agreement with the far more precise determination of Farnham *et al.* [68], and also with other previous measurements [12,79,80] (see Tab. 25).

Table 25. Determination of the proton-to-electron mass ratio.

	m_p/m_e	relative uncertainty
van Dyck *et al.* [79]	1 836.152 701(37)	2×10^{-8}
Garreau *et al.* [12]	1 836.152 59(24)	1.3×10^{-7}
Gabrielse *et al.* [80]	1 836.152 680(88)	4.8×10^{-8}
Farnham *et al.* [68]	1 836.152 6665(40)	2.2×10^{-9}
this work		
$\Delta_{H-D}(n = 8)$	1 836.152 668(115)	6.3×10^{-8}
$\Delta_{H-D}(n = 12)$	1 836.152 666(128)	7×10^{-8}
weighted mean	1 836.152 667(85)	4.6×10^{-8}

7 Conclusion

Thanks to a detailed analysis of the lineshapes of the 2S–nS/D transitions, we have obtained more reliable values of the $1S_{1/2}$ Lamb shift and of the $2S_{1/2}$–$nS_{1/2}$, –nD_J frequencies. These results have been analyzed with a least squares procedure, by taking into account several precise measurements from other groups. If we do not use the $1/n^3$ scaling law for the Lamb shift, the relative uncertainties in the Rydberg constant and the $1S_{1/2}$ Lamb shift are 10^{-11} and 3.8×10^{-6} respectively. In this case, the accuracy is limited mainly by the uncertainty in the $2S_{1/2}$ Lamb shift. To avoid this problem, we make theoretical assumptions concerning the Lamb shift. By using the $1/n^3$ scaling law between the $1S_{1/2}$ and $2S_{1/2}$ Lamb shifts, the very precise optical frequency measurements reduce the uncertainties to 9.1×10^{-12} and 3.2×10^{-6} for R_∞ and the Lamb shifts. By this means, we obtain a value of the $2S_{1/2}$ Lamb shift which is about 2.6 times more precise than the direct microwave measurement. Moreover, the same method can

be applied to deuterium. Finally, we average these different results to reduce the uncertainties in R_∞ and in the Lamb shifts to 7.7×10^{-12} and 2.7×10^{-6}. The precision is now limited by the uncertainties in the 2S–nS/D frequencies, which, in our experiment, are mainly due to the light shifts. To obtain more accurate values of these frequencies, a first possibility is to use ultracold hydrogen to increase the interaction time and decrease the light shifts [81]. In our group, we intend to measure the optical frequency of the 1S–3S transition. In this case, as the number of atoms in the 1S atomic beam is about 10^8 times larger than in the metastable atomic beam, we can observe the transition with a very small light power and, consequently, with negligible light shifts. For this experiment, we plan to compensate the second-order Doppler effect using a magnetic field perpendicular to the atomic beam [82]. As a last word, we note that a new determination of the proton radius r_p is highly desirable. The future measurement of r_p, being prepared at the Paul Scherrer Institute by spectroscopy of muonic hydrogen, should provide the opportunity to test even further the theoretical calculations of the Lamb shift [83].

The authors thank S. Bourzeix, M.D. Plimmer, F. de Tomasi and D.N. Stacey for their essential contribution to the first step of the 1S–3S experiment. They are indebted to B. Cagnac for many stimulating discussions as well as his constant interest in these projects. They thank also M. Pinard for fruitful discussions on the calculation of the theoretical line shape and D. Delande for his help in the use of the Sturmian functions and the calculation of several matrix elements of the two-photon and light shift operators. Finally, they thank again M.D. Plimmer for critical reading of manuscript. This work was partially supported by the Bureau National de Métrologie, by the Direction des Recherches et Études Techniques and by the European Community (SCIENCE cooperation Contract No. SCI*-CT92-0816 and network Contract No. CHRX-CT93-0105).

References

1. B. Cagnac, M.D. Plimmer, L. Julien, F. Biraben, Rep. Prog. Phys. **57**, 853 (1994).
2. Th. Udem, H. Huber, B. Gross, J. Reichert, M. Prevedelli, M. Weitz, T.W. Hänsch, Phys. Rev. Lett. **79**, 2646 (1997); note added in proof: a more accurate result has been recently published: J. Reichert, M. Niering, R. Holwarth, M. Weitz, Th. Udem, T.W. Hänsch, Phys. Rev. Lett. **84**, 3232 (2000).
3. A. Huber, Th. Udem, B. Gross, J. Reichert, M. Kourogi, K. Pachucki, M. Weitz, T.W. Hänsch, Phys. Rev. Lett. **80**, 468 (1998).
4. F. Nez, M.D. Plimmer, S. Bourzeix, L. Julien, F. Biraben, R. Felder, O. Acef, J.J. Zondy, P. Laurent, A. Clairon, M. Abed, Y. Millerioux, P. Juncar, Phys. Rev. Lett. **69**, 2326 (1992).
5. F. Nez, M.D. Plimmer, S. Bourzeix, L. Julien, F. Biraben, R. Felder, Y. Millerioux, P. de Natale, Europhys. Lett. **24**, 635 (1993).
6. B. de Beauvoir, F. Nez, L. Julien, B. Cagnac, F. Biraben, D. Touahri, L. Hilico, O. Acef, A. Clairon, J.J. Zondy, Phys. Rev. Lett. **78**, 440 (1997).
7. D. Touahri, O. Acef, A. Clairon, J.J. Zondy, R. Felder, L. Hilico, B. de Beauvoir, F. Biraben, F. Nez, Opt. Commun. **133**, 471 (1997).
8. C. Schwob, L. Jozefowski, B. de Beauvoir, L. Hilico, F. Nez, L. Julien, F. Biraben, O. Acef, A. Clairon, Phys. Rev. Lett. **82**, 4960 (1999).
9. S. Bourzeix, B. de Beauvoir, F. Nez, M.D. Plimmer, F. de Tomasi, L. Julien, F. Biraben, D.N. Stacey, Phys. Rev. Lett. 76, 384 (1996).
10. J.C. Garreau, M. Allegrini, L. Julien, F. Biraben, J. Phys. France **51**, 2263 (1990).
11. J.C. Garreau, M. Allegrini, L. Julien, F. Biraben, J. Phys. France **51**, 2275 (1990).
12. J.C. Garreau, M. Allegrini, L. Julien, F. Biraben, J. Phys. France **51**, 2293 (1990).
13. S. Bourzeix, M.D. Plimmer, F. Nez, L. Julien, F. Biraben, Opt. Commun. **99**, 89 (1993).
14. R.W.P. Drever, J.L. Hall, F.V. Kowalski, J. Hough, G.M. Ford, A.J. Munley, H. Ward, Appl. Phys. B **31**, 97 (1983).
15. F. Nez, Thèse de doctorat de l'université Pierre et Marie Curie, Paris, 1993.
16. F. Biraben, J.C. Garreau, L. Julien, M. Allegrini, Rev. Sci. Instrum. **61**, 1468 (1990).
17. T.W. Hänsch, B. Couillaud, Opt. Commun. **41**, 441 (1980).
18. B. Cagnac, G. Grynberg, F. Biraben, J. Phys. France **34**, 845 (1973).
19. D. Delande, private communication.
20. H.A. Bethe, E.E. Salpeter, in *Quantum mechanics of one- and two-electron atoms* (Springer-Verlag, Berlin, 1957).
21. W.J. Karzas, R. Latter, Astrophys. J. Suppl. Ser. **6**, 167 (1961).
22. G. Grynberg, B. Cagnac, F. Biraben, in *Coherent Nonlinear Optics*, edited by M.S. Feld, V.S. Letokhov (Springer-Verlag, 1980).
23. F. Biraben, M. Bassini, B. Cagnac, J. Phys. France **40**, 445 (1979).
24. J.W. Farley, W.H. Wing, Phys. Rev. A **23**, 2397 (1981).
25. B. de Beauvoir, Thèse de doctorat de l'université Pierre et Marie Curie, Paris, 1996.
26. Y Millerioux, D. Touahri, L. Hilico, A. Clairon, R. Felder, F. Biraben, B. de Beauvoir, Opt. Commun. **103**, 91 (1994).
27. L. Hilico, R. Felder, D. Touahri, O. Acef, A. Clairon, F. Biraben, Eur. Phys. J. AP **4**, 219 (1998).
28. B. de Beauvoir, F. Nez, L. Hilico, L. Julien, F. Biraben, B. Cagnac, J.J. Zondy, D. Touahri, O. Acef, A. Clairon, Eur. Phys. J. D **1**, 227 (1998).
29. A. Clairon, B. Dahmani, A. Filimon, J. Rutman, IEEE Trans. Inst. Meas. **IM34**, 265 (1985).
30. A. Clairon, B. Dahmani, O. Acef, M. Granveaud, Y.S. Domnin, S.B. Pouchkine, V.M. Tatarenkov, R. Felder, Metrologia **25**, 9 (1988).
31. G.D. Rovera, O. Acef, IEEE Trans. Inst. Meas. **48,** 571 (1999).
32. F. Nez, M.D. Plimmer, S. Bourzeix, L. Julien, F. Biraben, R. Felder, Y. Millerioux, P. de Natale, IEEE Trans. Inst. Meas. **44,** 568 (1995).
33. O. Acef, J.J. Zondy, M. Abed, G.D. Rovera, A.H. Gerard, A. Clairon, P. Laurent, Y. Millerioux, P. Juncar, Opt. Commun. **97**, 29 (1993).
34. F. Nez, F. Biraben, R. Felder, Y. Millerioux, Opt. Commun. **102**, 432 (1993).

35. R. Felder, D. Touahri, O. Acef, L. Hilico, J.J. Zondy, A. Clairon, B. de Beauvoir, F. Biraben, F. Nez, L. Julien, Y. Millerioux, Proc. SPIE **2378**, 52 (1995).
36. J.W. Heberle, H.A. Reich, P. Kusch, Phys. Rev. **101**, 612 (1956).
37. G.W.F. Drake, R.A. Swainson, Phys. Rev. A **41**, 1243 (1990).
38. J.R. Sapirstein, D.R. Yennie, in *Quantum Electrodynamics*, edited by T. Kinoshita (World Scientific, Singapore, 1990).
39. P.J. Mohr, in *Atomic, Molecular and Optical Physics Handbook*, edited by G.W.F. Drake (AIP, New-York, 1996).
40. K. Pachucki, D. Leibfreid, M. Weitz, A. Huber, W. Köning, T.W. Hänsch, J. Phys. B **29**, 177 (1996).
41. G.G. Simon, C. Schmitt, F. Borkovski, V.H. Walther, Nucl. Phys. A **333**, 381 (1980).
42. M. Weitz, A. Huber, F. Schmidt-Kaler, D. Leibfreid, W. Vassen, C. Zimmermann, K. Pachucki, T.W. Hänsch, L. Julien, F. Biraben, Phys. Rev. A **52**, 2664 (1995).
43. H.A. Reich, J.W. Heberle, P. Kusch, Phys. Rev. **104**, 1585 (1956).
44. P.J. Mohr, B.N. Taylor, Rev. Mod. Phys. **72** (to be published, 2000).
45. C. Schwob, L. Jozefowski, O. Acef, L. Hilico, B. de Beauvoir, F. Nez, L. Julien, A. Clairon, F. Biraben, IEEE Trans. Inst. Meas. **48**, 178 (1999).
46. H.R. Telle, D. Meschede, T.W. Hänsch, Opt. Lett. **15**, 532 (1990).
47. T.W. Hänsch, S.A. Lee, R. Wallenstein, C. Wieman, Phys. Rev. Lett. **34**, 307 (1975)
48. M.G. Boshier, P.E.G. Baird, C.J. Foot, E.A. Hinds, M.D. Plimmer, D.N. Stacey, J.B. Swan, D.A. Tate, D.M. Warrington, G.K. Woodgate, Nature **330**, 463 (1987); Phys. Rev. A **40**, 6169 (1989).
49. M. Weitz, A. Huber, F. Schmidt-Kaler, D. Leibfreid, T.W. Hänsch, Phys. Rev. Lett. **72**, 328 (1994).
50. D.J. Berkeland, E.A. Hinds, M.G. Boshier, Phys. Rev. Lett. **75**, 2470 (1995).
51. S. Bourzeix, B. de Beauvoir, F. Nez, F. de Tomasi, L. Julien, F. Biraben, Opt. Commun. **133**, 239 (1997).
52. K.C. Harvey, C. Fehrenbach, Rev. Sci. Instrum. **54**, 1117 (1983).
53. Y. Gontier, M. Trahin, Phys. Lett. A **36**, 463 (1971).
54. U.D. Jentschura, P.J. Mohr, G. Soff, Phys. Rev. Lett. **82**, 53 (1999).
55. K. Pachucki, Phys. Rev. Lett. **72**, 3154 (1994).
56. S. Mallampalli, J. Sapirstein, Phys. Rev. Lett. **80**, 5297 (1998).
57. I. Goidenko, L. Labzowsky, A. Nefiodov, G. Plunien, G. Soff, Phys. Rev. Lett. **83**, 2312 (1999).
58. L.N. Hand, D.J. Miller, R. Wilson, Rev. Mod. Phys. **35**, 335 (1963).
59. S.G. Karshenboim, J. Phys. B **29**, L29 (1996); Z. Phys. D **39**, 109 (1997).
60. W.E. Lamb, R.C. Retherford, Phys. Rev. **72**, 241 (1947).
61. S.R. Lundeen, F.M. Pipkin, Phys. Rev. Lett. **46**, 232 (1981).
62. E.W. Hagley, F.M. Pipkin, Phys. Rev. Lett. **72**, 1172 (1994).
63. U. Jentschura, K. Pachucki, Phys. Rev. A **54**, 1853 (1996).
64. A. van Wijngaarden, F. Holuj, G.F.W. Drake, Can. J. Phys. **76**, 95 (1998).
65. V.G. Pal'chikov, Y.L. Sokolov, V.P. Yakovlev, Metrologia **21**, 99 (1985); Phys. Scripta **55**, 33 (1997).
66. V.G. Pal'chikov, Y.L. Sokolov, V.P. Yakovlev, Sov. Phys. JETP Lett. **38**, 419 (1983).
67. S.G. Karshenboim, Sov. Phys. JETP **79**, 230 (1994).
68. D.L. Farnham, R.S. van Dyck Jr, P.B. Schwinberg, Phys. Rev. Lett. **75**, 3598 (1995).
69. G. Audi, A.H. Wapstra, Nucl. Phys. A **565**, 1 (1993).
70. E.R. Cohen, B.N. Taylor, Rev. Mod. Phys. **59**, 1121 (1987).
71. F. Biraben, J.C. Garreau, L. Julien, Europhys. Lett. **2**, 925 (1986).
72. P. Zhao, W. Lichten, H.P. Layer, J.C. Bergquist, Phys. Rev. A **34**, 5138 (1986).
73. P. Zhao, W. Lichten, H.P. Layer, J.C. Bergquist, Phys. Rev. Lett. **58**, 1293 (1987).
74. D.H. Mc Intyre, R.G. Beausoleil, C.J. Foot, E.A. Hildum, B. Couillaud, T.W. Hänsch, Phys. Rev. A **39**, 4591 (1989).
75. F. Biraben, J.C. Garreau, L. Julien, M. Allegrini, Phys. Rev. Lett. **62**, 621 (1989).
76. T. Andreae, W. Köning, R. Wynands, D. Leibfried, F. Schmidt-Kaler, C. Zimmermann, D. Meschede, T.W. Hänsch, Phys. Rev. Lett. **69**, 1923 (1992).
77. G. Newton, D.A. Andrews, P.J. Unsworth, Philos. Trans. R. Soc. Lond. **290**, 373 (1979).
78. B.L. Cosens, Phys. Rev. **173**, 49 (1968).
79. R.S. van Dyck, F.L. Moore, D.L. Farnham, P.B. Schwinberg, Bull. Am. Phys. Soc. **31**, 244 (1986).
80. G. Gabrielse, X. Fei, L.A. Orozco, R.L. Tjoelker, J. Haas, H. Kalinowsky, T.A. Trainor, W. Kells, Phys. Rev. Lett. **65**, 1317 (1990).
81. C.L. Cesar, D.G. Fried, T.C. Killian, A.D. Polcyn, J.C. Sandberg, I.A. Yu, T.J. Greytak, D. Kleppner, J.M. Doyle, Phys. Rev. Lett. **77**, 255 (1996).
82. F. Biraben, L. Julien, J. Plon, F. Nez, Europhys. Lett. **15**, 831 (1991).
83. D. Taqqu, F. Biraben, C.A.N. Conde, T.W. Hänsch, F.J. Hartmann, P. Hauser, P. Indelicato, P. Knowles, F. Kottmann, F. Mulhauser, C. Petitjean, R. Pohl, P. Rabinowitz, R. Rosenfelder, J.M.F. Santos, W. Schott, L.M. Simons, J. Veloso, Hyperfine Interact. **119**, 311 (1999).